



Article

ANN-Based Maximum Power Tracking for a Grid-Synchronized Wind Turbine-Driven Doubly Fed Induction Generator Fed by Matrix Converter

Mohamed A. Alarabi and Sedat Sünter *

Electrical and Electronics Engineering Department, Atilim University, Ankara 06830, Türkiye; malarabi1991@gmail.com or alarabi.maarelbi@student.atilim.edu.tr

* Correspondence: sedat.sunter@atilim.edu.tr

Abstract: The integration of renewable energy sources, such as wind power, into the electrical grid is essential for the development of sustainable energy systems. Doubly fed induction generators (DFIGs) have been significantly utilized in wind energy conversion systems (WECSs) because of their efficient power generation and variable speed operation. However, optimizing wind power extraction at variable wind speeds remains a major challenge. To address this, an artificial neural network (ANN) is adopted to predict the optimal shaft speed, ensuring maximum power point tracking (MPPT) for a wind energydriven DFIG connected to a matrix converter (MC). The DFIG is controlled via field-oriented control (FOC), which allows independent power output regulation and separately controls the stator active and reactive power components. Through its compact design, bidirectional power flow, and enhanced harmonic performance, the MC, which is controlled by the simplified Venturini modulation technique, improves the efficiency and dependability of the system. Simulation outcomes confirm that the ANN-based MPPT enhances the power extraction efficiency and improves the system performance. This study shows how wind energy systems can be optimized for smart grids by integrating advanced control techniques like FOC and simplified Venturini modulation with intelligent algorithms like ANN.

Keywords: wind energy; WECS; MPPT; DFIG; FOC; MC; Venturini algorithm



Academic Editors: Ke Xu and Yuan Liao

Received: 8 April 2025 Revised: 5 May 2025 Accepted: 9 May 2025 Published: 13 May 2025

Citation: Alarabi, M.A.; Sünter, S. ANN-Based Maximum Power Tracking for a Grid-Synchronized Wind Turbine-Driven Doubly Fed Induction Generator Fed by Matrix Converter. *Energies* 2025, *18*, 2521. https://doi.org/10.3390/en18102521

Copyright: © 2025 by the authors. Licensee MDPI, Basel, Switzerland. This article is an open access article distributed under the terms and conditions of the Creative Commons Attribution (CC BY) license (https://creativecommons.org/licenses/by/4.0/).

1. Introduction

In the last two decades, wind energy has definitively been recognized as an applicable source of renewable energy systems, fundamentally due to its characteristic of being an inexhaustible source that could be converted to electrical energy across numerous systems called WECSs. Recently, researchers have increasingly concentrated on the optimization of WECSs to take advantage of the full potential of this abundant and non-polluting energy source [1]. Furthermore, nowadays, energy experts are looking for alternative efficacious and environmentally friendly energy resources in order to decrease the dependence on fossil fuels such as hydrocarbon- and petroleum-based fuels, the primary contributor to the problem of global warming, which are becoming scarce [2]. The increasing integration of the production of wind energy in modern power systems has brought about new difficulties and challenges. One of the significant requirements for WECSs is their capability for generating stable and desirable power in spite of fluctuating and varying wind speed situations; moreover, they react swiftly to sudden wind speed variations [3]. Numerous control schemes have been suggested for both grid-side converters and machine-side converters,

Energies **2025**, 18, 2521 2 of 25

interconnected through a DC bus capacitor. Additionally, WECSs use a range of electrical generator types, such as permanent magnet synchronous generators (PMSG) and DFIG, to effectively convert wind energy into electrical energy [4]. Fixed-speed and variable-speed WECSs are the two main categories into which WECSs have been divided according to their operational speed. In fixed-speed WECSs, power converters are not required because of the constancy in the speed of the generator's rotor and the direct connection to the grid [5]. In the variable-speed WECSs, in order to make sure that the turbine runs at its maximum power, the generator's shaft speed needs to be continuously modified and adjusted. As a result, the maximum power extraction (MPE) occurs, which would be the cause of the rising annual production of the energy by 5–10% [6]. Taking into consideration that the wind turbine operating regions have been divided into four operation regions presented in Figure 1, the first region encompasses the area from start-up until the cut-in point. The second region, commonly referred to as the MPPT region, spans between the cut-in and the rated speed, where the turbine's output power ought to be maximized. The third region, known as the speed regulation region, aims to keep the shaft speed at rated levels in order to ensure that the turbine does not generate power exceeding the generator's rated capacity. The fourth region occurs if the speed of the wind exceeds the cut-out point, ensuring protection against potential damage from excessively high wind speeds [2,4]. It is remarkable to note that the maximum power from WECSs can be taken out by operating the turbine in the second region [7].

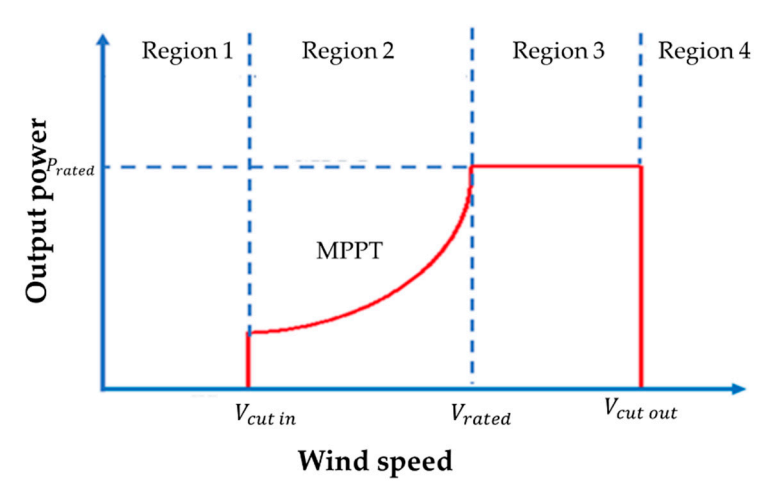


Figure 1. The wind turbine's operational regions.

To optimize the efficiency and performance, several algorithms have been applied in WECSs. Among them is the MPPT algorithm, which is widely utilized in sustainable energy systems, such as photovoltaic systems and wind energy, to maximize power extraction under varying environmental conditions [8]. In WECSs, the MPPT algorithm's primary objective is to gather the greatest possible amount of power from the wind. The two primary methods, into which MPPT algorithms have been separated in the published works, are direct power control (DPC) and indirect power control (IPC) [9]. DPC directly measures the generated output power and modifies system parameters to guarantee that the turbine performs its MPE. In contrast, the IPC technique pre-calculates the power using wind-speed data [3,8,9].

WECSs, equipped with variable-speed wind turbine-driven DFIGs, have been becoming widespread day by day due to their capability of operating throughout a broad spectrum of fluctuating wind speeds and can be operated at both sub-synchronous and super-synchronous speeds. Moreover, they can be controlled with a partial-scale converter since the converter addresses only the slip power, so that the converter components can

Energies **2025**, 18, 2521 3 of 25

be smaller and less expensive compared to those in full-power conversion systems. Typically, a gearbox is used to operate the DFIG, creating a link between the wind turbine and the DFIG [10-12].

WECSs are characterized by an environmentally friendly nature and low-cost installation, yet they often suffer from low efficiency because of continuously altering wind speeds [13]. Therefore, the MPPT plays a critical role in enhancing WECSs' performance. Various significant studies have been conducted to improve efficient MPPT controllers; many of them have been applied to variable speed DFIGs, which can continuously become acclimatized to changing wind speeds. This acclimation has been leading to an enhancement in the overall turbine efficiency and limited power fluctuations [14]. MPPT's fundamental objective is to maximize the power coefficient's value (Cp) to its highest value, even with fluctuations in wind speed. The existing literature covers two broad methods of MPPT strategies, which are conventional methods and the soft computingbased approach [2]. Hill climbing search (HCS), which has been also known as perturbation and observation (P&O), is one of the conventional techniques that has been documented in [15]. One more method is the optimal torque control (OTC) technique, and it is utilized to maximize the power for a WECS-based PMSG [16]. The advantages of this technique are higher efficiency and straightforwardness. However, it suffers from dependency on the climatic conditions [9]. Latterly, many researchers have been interested in soft computing approaches, divided into two categories: nature-inspired techniques and artificial intelligence (AI) techniques [2]. Ant colony optimization (ACO) [17], particle swarm optimization (PSO) [18], and genetic algorithms (GAs) [19] are a few of the nature-inspired methods adopted into the MPPT controller. Compared to conventional methods, the nature-inspired methods have demonstrated fast tracking under changeable wind speeds. However, the requirements of the multiparameter-like selection of chromosomes, crossover rate, and population size have made them complex tasks [20]. The AI-based MPPT controller in WECSs involves a fuzzy logic (FL) controller [21,22] and an ANN-based controller [23,24]. These methods do not require accurate mathematical modeling even though they operate with variable inputs and have the ability of self-convergence in addition to self-learning capabilities. Moreover, they are adaptable to the systems' non-linear behavior. The FL technique has been used for maximizing the extracted power in WECSs [21,22]. However, its tracking performance and efficiency depend on the predefined rule base, which decreases its practical applicability. In addition, it requires a large scale of hypothetical knowledge and might not ensure the best possible response [2]. In [23], the ANN technique was utilized for pitch angle controllers to enhance the power maximization from the available wind in a grid-connected wind turbine system. The outcomes demonstrated that the controllerbased ANN has better performance in contrast against traditional strategies.

In [25], in order to control DFIG-based-WECS, MPPT control based on the adaptive neuro-fuzzy inference (ANFI) method was employed. The simulation results of the ANFI-based approach were compared with those obtained using a classical PI controller. The frequently used method in WECSs is the sliding mode control (SMC) method. It offers robustness with variations in system parameters and can effectively handle limited external disturbances. Thus, it has been widely utilized to control the squirrel cage induction generator [26]. It has been reported in [27] that the fractional-order PI controller method has been utilized for controlling the pitch angle, and the simulation results demonstrated an enhancement in the capacity of DFIG at strong wind conditions. Other control methods have been also reported in the literature, such as the proportional integral [28], the linear-quadratic-Gaussian control method [29], and quantitative feedback theory [30], which have been used for the MPPT of WECSs. However, such methods seek inclusive computational

Energies **2025**, 18, 2521 4 of 25

and graphical analysis and because they are not robust, they often result in oscillations at output power [31].

It is essential for variable-speed WECSs to convert power from a source with varying speed into electrical energy with a consistent frequency. In a variable-speed WECS that uses DFIG, the main grid is directly connected to the stator side windings, so that fixed-frequency electric power can be generated through the stator side, whereas the windings of the rotor are supplied with inconstant voltage and frequency. To integrate the rotor-side with the main grid, a controllable power electronic converter is required [10]. Additionally, effective speed control is required to achieve MPT [11].

Grid-connected variable-speed WECSs driven by DFIG typically employ a back-to-back converter that enables bidirectional power flow [32]. However, back-to-back converters involve two-stage power conversion, which might require a complex control algorithm to control the entire system effectively. Moreover, the large DC link capacitors which are used in the converter system may increase volume, weight, and cost [33].

The DFIG can be controlled by a direct AC-AC MC in place of a traditional back-to-back converter. The MC has a number of positive effects, including the ability to guarantee sinusoidal input, output currents, and bidirectional power flow in a single-stage conversion process without the necessity for a DC link capacitor. It has also gained popularity because of its unity input power factor. Unlike traditional back-to-back converters, the MC has a simpler control strategy and does not seek large and expensive elements for energy storing. Furthermore, it can extend the speed range of the DFIG to be operated over synchronous speed, so that the DFIG can deliver power not only from the stator but also from the rotor to the main grid through MC. All the above-mentioned advantages have made the MC a perfect choice for the wind power generation systems [34,35]. Most control strategies for wind turbine-driven DFIG systems are typically based on the FOC approach [10,36].

In DFIG-based WECSs, the FOC schematic is specifically designed to regulate the rotor currents in such a way that the power can flow bidirectionally from and to the grid, depending on the rotor speed and operation conditions. This approach allows the shaft speed to follow the reference value, which is determined by the curves of power-speed characteristic of the wind turbine [10]. A block diagram of a grid-connected DFIG-based WECS with MC is illustrated in Figure 2.

The ANN-based MPPT strategies have been discussed for several renewable energy systems in the literature. However, no prior study has combined an ANN-based MPPT approach with a MC-fed DFIG for a WECS. The proposed control strategy, which has been presented in [10], uses a 2D lookup table for achieving the MPPT in a DFIG-based WECS with a MC. While effective, the 2D lookup table method seeks offline data and lacks adaptation to unexpected operating conditions. To address these limitations, this study proposes replacing the 2D lookup table with an ANN-based MPPT approach, offering improved adaptability, dynamic response, and reduced reliance on offline-generated data. This paper presents the design, simulation, and evaluation of the proposed ANN-based MPPT strategy.

The main contributions of this study are summarized as follows: proposing an ANN-based MPPT approach to replace the conventional 2D lookup table utilized in reference [10]; integrating the ANN-based MPPT with the FOC strategy in a DFIG-based WECS fed by an MC, which ensures bidirectional power flow with unity power factor; developing a global simulation model in MATLAB/Simulink (version: R2024a)to evaluate the proposed system under different wind conditions; and providing a comparative analysis of the ANN and the 2D lookup table approach from [10].

Energies **2025**, 18, 2521 5 of 25

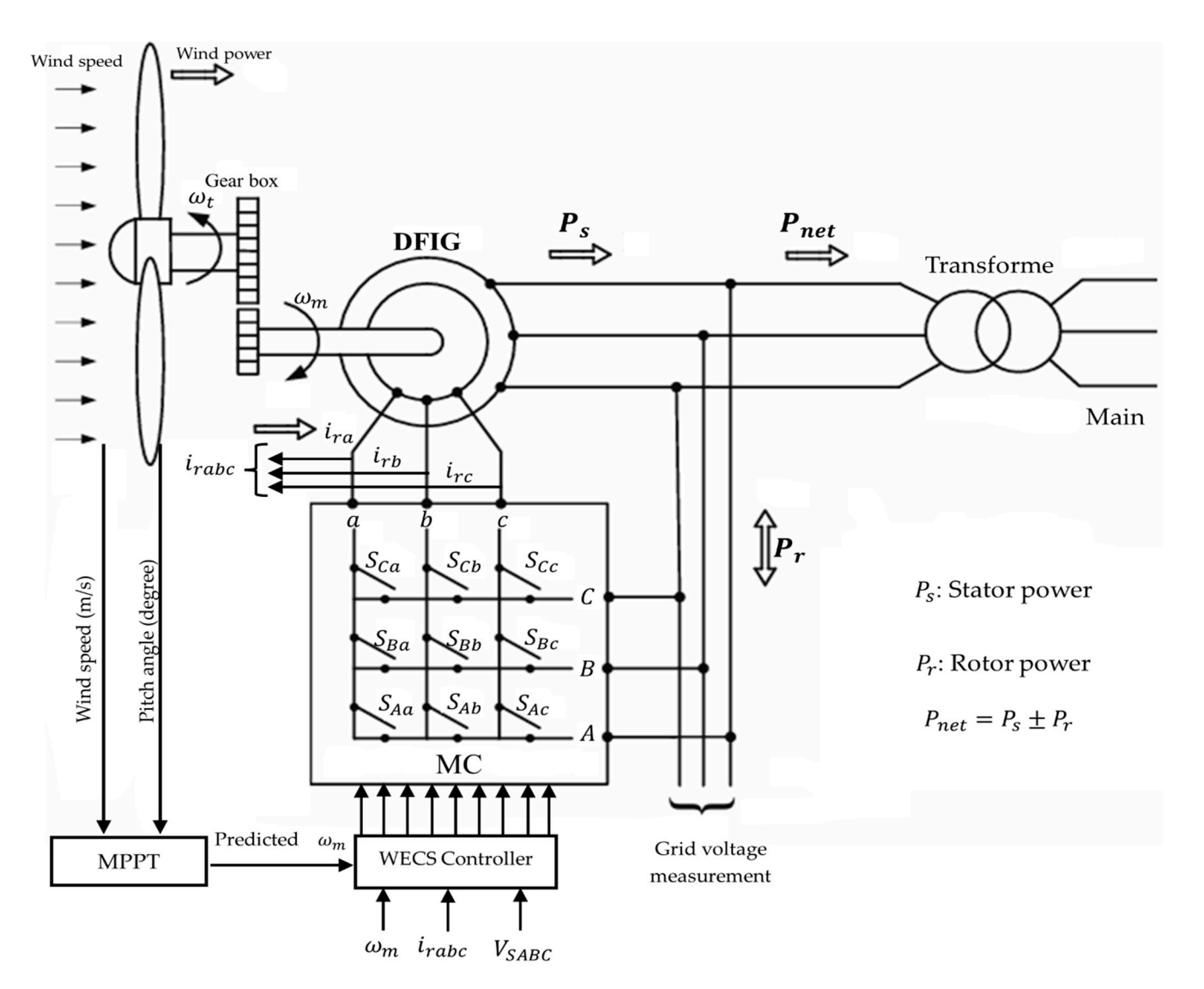


Figure 2. The diagram of a variable-speed WECS.

2. Wind Turbine Model

The produced power and mechanical torque, both of which depend on the airflow across the blades and are significantly influenced by varying wind speeds, are represented by the wind turbine's aerodynamic model [3]. The mechanical power on the turbine's rotor is influenced by the power coefficient $C_p(\lambda,\theta)$, which varies with wind speed (v_w) in $\frac{m}{s}$ and blade pitch angle (θ) in degrees, can be expressed as follows [10,37]:

$$P_{w} = \frac{1}{2} C_{p}(\lambda, \theta) \rho \pi R^{2} v_{w}^{3}$$
 (1)

where *R* is the turbine rotor-plane radius (m); ρ is the air density $\left(\frac{K_g}{m^3}\right)$; and λ is the tip speed ratio, which is calculated by Equation (2):

$$\lambda = \frac{\omega_t R}{v_w} \tag{2}$$

Equation (3) gives the generated mechanical torque by the turbine:

$$T_t = \frac{P_w}{\omega_t} \tag{3}$$

Energies **2025**, 18, 2521 6 of 25

where ω_t is the turbine shaft's speed in $\frac{rad}{s}$. The mechanical coupling between the generator and turbine is commonly achieved by a gearbox, whose ratio G is calculated as Equation (4):

 $G = \frac{\omega_m}{\omega_t} \tag{4}$

where ω_m is the generator speed $\frac{rad}{s}$. If the power obtained from the wind turbine overrides the generator's rated power, limiting the wind turbine's input power is essential and pitch angle control achieves this. However, when the obtained power in a range below the generator-rated power, the turbine ought to extract the maximum amount of power [10,38]. It should be noted that the power coefficient $C_p(\lambda,\theta)$ is at its highest level when the pitch angle value is zero.

$$C_p(\lambda, \theta) = 0.22 \left(\frac{116}{\lambda_i} - 0.4 \theta - 5\right) e^{-\frac{12.5}{\lambda_i}}$$
 (5)

$$\frac{1}{\lambda_i} = \frac{1}{\lambda + 0.08 \,\theta} - \frac{0.035}{1 + \theta^3} \tag{6}$$

As illustrated in Figure 3, the output power of the turbine is shown remarkably and simultaneously rising as the speed of the wind rises. It is also obvious that the curve of the output power attains its peak value at a definite shaft speed. Therefore, the turbine should be run at the speed value that maximizes the power. Keep in mind that the value of C_p , which is a non-linear function of tip speed ratio λ and pitch angle θ , differs depending on the system. Theoretically, the highest value of C_p is 0.44, as depicted in Figure 4 [10]. The mathematical details of C_p is found in [39].

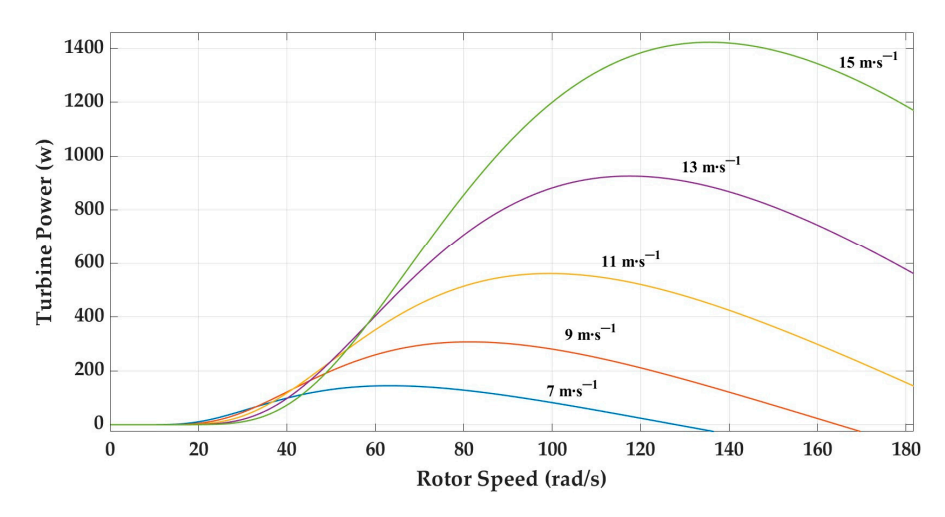


Figure 3. The turbine characteristics in terms of power and speed for varying wind speeds.

The wind turbine characteristics shown in Figures 3 and 4 were drawn based on Equations (2), (5) and (6).

In this paper, the pitch angle control not only regulates the aerodynamic power input at high wind speeds but also acts as an inherent rotor speed-limiting mechanism by reducing the aerodynamic torque. As a result, there was no need for a separate speed limiter in the control system. This interaction was embedded in the training data of the ANN, where the pitch angle values reflect both normal operation and power-limiting conditions. Accordingly, the ANN was trained to predict the optimal shaft speed based on both wind speed and pitch angle.

The wind turbine model represents a laboratory-scale turbine that has been designed to align with the characteristics of the 1 kW DFIG, which is available in the laboratory, ensuring compatibility for the simulation and potential experimental validation.

Energies **2025**, 18, 2521 7 of 25

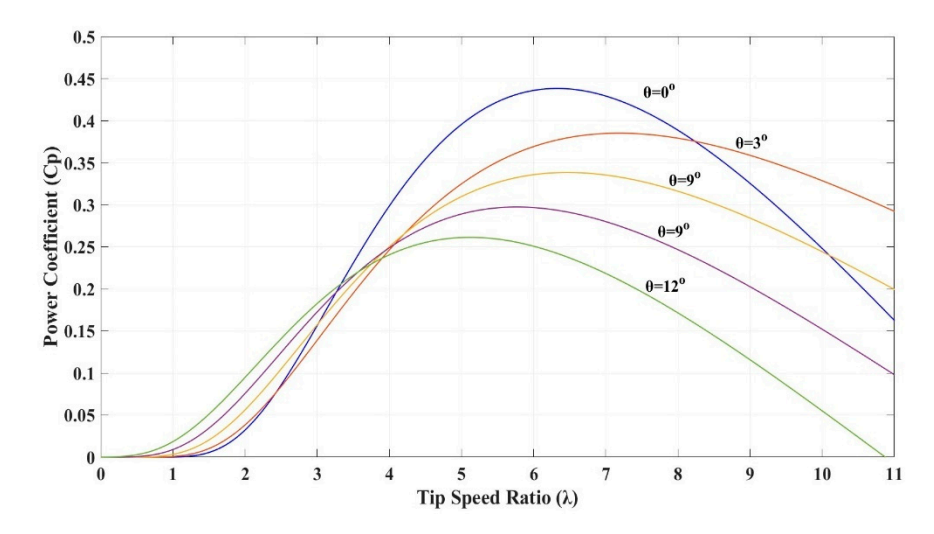


Figure 4. The turbine's characteristics at different wind speeds.

3. The MC and Simplified Form of Venturini Algorithm

The MC, which consists of bidirectional switches, functions as a direct AC-AC converter. It has the ability to convert an input voltage with a constant amplitude and frequency to a variable output voltage at different frequencies, and it eliminates the requirement of the intermediate DC link capacitor. Consequently, it provides a substitute solution to the conventional back-to-back converter, which is ordinarily and traditionally utilized to efficiently control the DFIG-based WECSs. The array of nine bi-directional switches, made up from semiconductor materials, establishes a direct connection between the three-phase source and the three-phase load, forming the direct three-phase AC-AC conversion. Figure 5 illustrates the schematic representation of MC where three groups of bi-directional switches have been coordinated; each group is connected with an output line. This coordination would provide a direct connection between the input and output phases [40–42]. Due to the direct supply of the MC from source voltage, it is imperative to keep away from short circuiting the input phase. Additionally, the output phase ought never to be open circuited if the load is inductive. For the MC to be operated safely, these two guidelines are necessary [42].

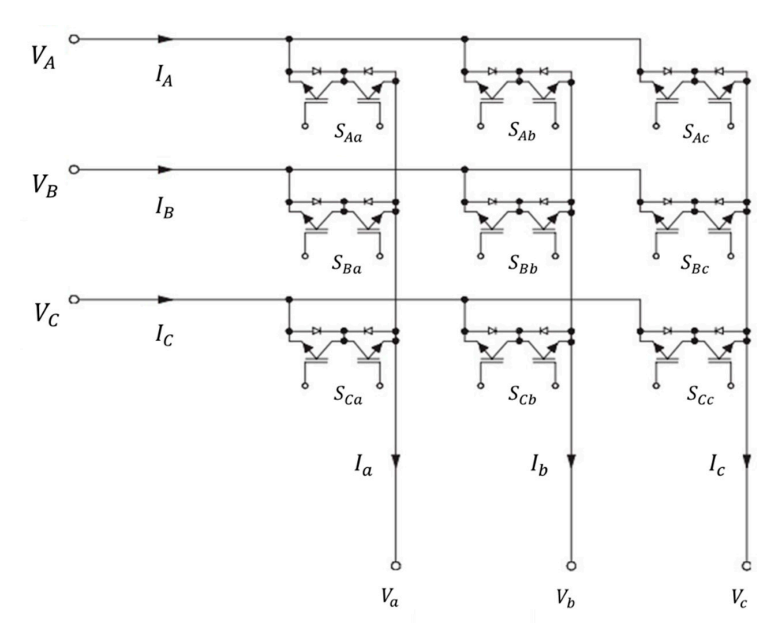


Figure 5. The power circuit for the MC.

Energies **2025**, 18, 2521 8 of 25

In this study, a simplified form of the Venturini modulation algorithm (Sunter–Clare algorithm) [43], has been used to control the MC. Implementation of this algorithm is easier and more appropriate for closed-loop operations. It is supposed that the MC is supplied by a balanced three-phase constant voltage source. The input voltages v_A , v_B , v_C , and modulation terms can be used to represent the MC output voltages v_a , v_b , v_c as in Equation (7).

$$\begin{bmatrix} v_a \\ v_b \\ v_c \end{bmatrix} = \begin{bmatrix} M_{Aa} & M_{Ba} & M_{Ca} \\ M_{Ab} & M_{Bb} & M_{Cb} \\ M_{Ac} & M_{Bc} & M_{Cc} \end{bmatrix} \begin{bmatrix} v_A \\ v_B \\ v_C \end{bmatrix}$$
(7)

To use this modulation technique, at least two of the three input line-to-line voltages need to be measured. Then, the peak value of input voltages V_{im} and its position ω_{it} can be expressed as Equation (8):

$$V_{im}^2 = \frac{4}{9} \left[V_{AB}^2 + V_{BC}^2 + V_{AB} V_{BC} \right] \tag{8}$$

$$\omega_i t = atan\left(\frac{V_{BC}}{\sqrt{3}\left(\frac{2V_{AB}}{3} + \frac{V_{BC}}{3}\right)}\right) \tag{9}$$

where V_{AB} , V_{BC} are the line voltages. The target voltage's peak magnitude, V_{om} and its position, ω_{ot} can be calculated by Equations (10) and (11):

$$V_{om}^2 = \frac{2}{3} \left[V_a^2 + V_b^2 + V_c^2 \right] \tag{10}$$

$$\omega_o t = \arctan\left(\frac{V_b - V_c}{\sqrt{3} V_a}\right) \tag{11}$$

where the target phase output voltages are denoted by V_a , V_b , and V_c . The voltage magnitude and angle are directly derived from the output of the control loops. Equation (12) is used to obtain the voltage ratio q:

$$q = \sqrt{\frac{V_{om}^2}{V_{im}^2}} \tag{12}$$

Note that the maximum value of q cannot exceed 0.866. Equations (13)–(15) are used to obtain the modulations for the output phase, a:

$$M_{Aa} = \frac{1}{3} + K_{31} + \frac{2}{3V_{im}^2} (V_a + K_{33}) \left(\frac{2V_{AB}}{3} + \frac{V_{BC}}{3} \right)$$
 (13)

$$M_{Ba} = \frac{1}{3} + K_{32} + \frac{2}{3V_{im}^2} (V_a + K_{33}) \left(\frac{V_{BC}}{3} - \frac{V_{AB}}{3} \right)$$
 (14)

$$M_{Ca} = 1 - (M_{Aa} + M_{Ba}) (15)$$

The triple harmonics K are injected into the target output voltage in order to achieve the maximum voltage ratio [44], and can be found using Equations (16)–(18):

$$K_{31} = \frac{2q}{9q_m} \sin(\omega_i t) \sin(3\omega_i t) \tag{16}$$

$$K_{32} = \frac{2q}{9q_m} \sin\left(\omega_i t - \frac{2\pi}{3}\right) \sin(3\omega_i t) \tag{17}$$

$$K_{33} = -\sqrt{V_{om}^2} \left[\frac{1}{6} \cos(3\omega_o t) - \frac{1}{4q_m} \cos(3\omega_i t) \right]$$
 (18)

Energies **2025**, 18, 2521 9 of 25

where q_m is the highest value of transfer ratio which equals to 0.866.

Based on Equations (13)–(18), for the unity power factor, the turn-on times of the switch locate between the input phase and the output phase are expressed as Equation (19).

$$T_{\beta\gamma} = T_s \left[\frac{1}{3} + \frac{2V_{o\gamma}V_{i\beta}}{3V_{im}^2} + \frac{2q}{9q_m} \sin\left(\omega_i t + \emptyset_\beta\right) \sin(3\omega_i t) \right]$$
(19)

where $V_{o\gamma}$ and $V_{i\beta}$ are the output and input voltages and can be calculated as follows:

$$V_{o\gamma} = qV_{im}.\cos(\omega_o t + \emptyset_{\gamma}) - \frac{q}{6}V_{im}\cos(3\omega_o t) + \frac{1}{4}\frac{q}{q_m}V_{im}\cos(3\omega_i t), V_{i\beta} = V_{im}\cos(\omega_i t + \emptyset_{\beta})$$
(20)

where \varnothing_{γ} , $\varnothing_{\beta} = 0, \frac{2\pi}{3}, \frac{4\pi}{3}$.

In Equations (13) and (14), V_a is substituted with V_b and V_c , respectively, to yield the modulation functions for phases b and c. It should be mentioned that the target output waveforms in Equation (10) do not have to be strictly sinusoidal. Equation (19) can be used to obtain the MC's input currents.

$$\begin{bmatrix} I_A \\ I_B \\ I_C \end{bmatrix} = \begin{bmatrix} M_{Aa} & M_{Ba} & M_{Ca} \\ M_{Ab} & M_{Bb} & M_{Cb} \\ M_{Ac} & M_{Bc} & M_{Cc} \end{bmatrix} \begin{bmatrix} I_a \\ I_b \\ I_c \end{bmatrix}$$
(21)

Switching signals for the MC were produced using a simplified version of the Venturini modulation method. The MC provides the controlled rotor voltage and frequency required to carry out FOC and decoupled active and reactive power regulation of the DFIG, taking the role of the traditional rotor-side back-to-back converter in this system. The MC supports the active and reactive control techniques used in this work as well as the MPPT by allowing bidirectional power flow and variable-frequency operation at the rotor side.

MC Model

MC has been modeled in MATLAB/Simulink as a switching-based model employing nine bidirectional switches coordinated in a 3×3 matrix arrangement. The FOC strategy has generated reference voltage signals to synthesize the required voltage and frequency for the rotor side. The simulation model operates the MC at a switching frequency of 5 kHz. Figure 6 illustrates the implementation of one phase of MC in Simulink. The other two phases are not shown for clarity since they are the same except for a phase shift of $\frac{2\pi}{3}$ and $\frac{4\pi}{3}$ [44]. Ideal switches have been assumed in the simulation of the MC circuit. Figure 7 shows in detail the switching period calculation of phase (a) using a simplified form of Venturini algorithm.

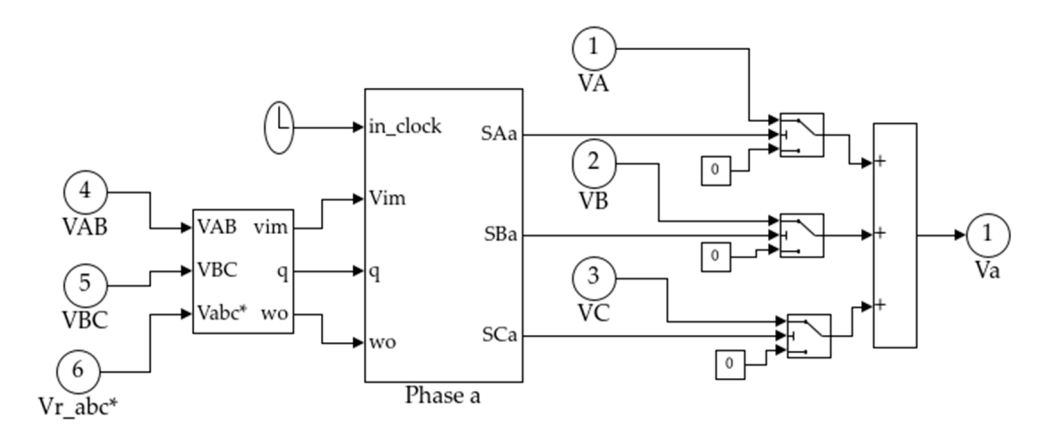


Figure 6. Detail of the Simulink block diagram of the MC for one phase.

Energies **2025**, 18, 2521 10 of 25

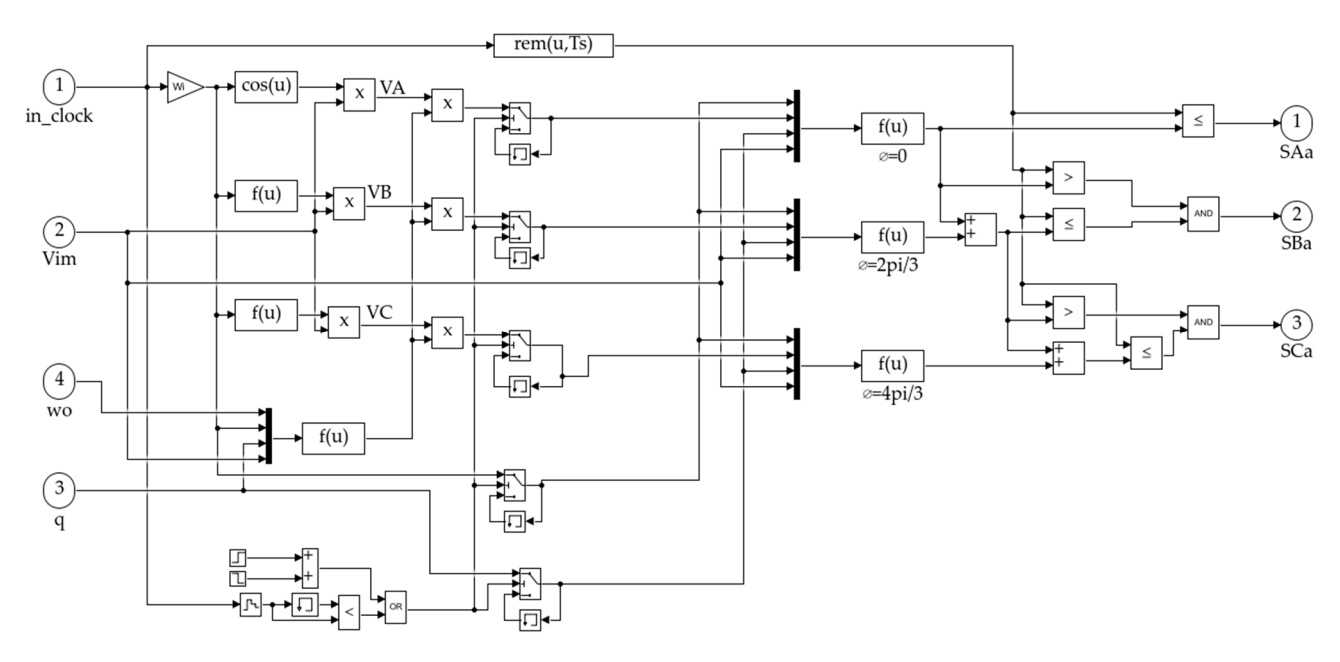


Figure 7. Switching period calculation of phase (a) using simplified form of Venturini algorithm.

In the Simulink block diagrams "*" refers to the reference values.

4. Dynamic Model of DFIG

The DFIG equivalent circuit in the d-q frame is displayed in Figure 8. All the machine parameters are referred to the stator side. This approach simplifies the machine structure and allows us to easily simulate the machine in closed-loop control systems [3].

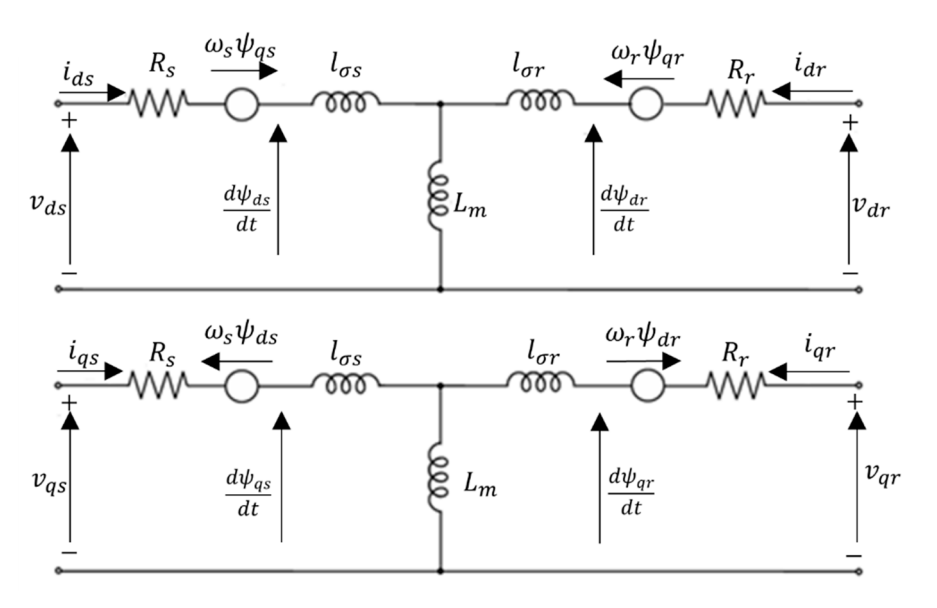


Figure 8. The equivalent circuit of DFIG in d - q frame.

Equations (22)–(29) represent the DFIG model in the synchronously rotating d-q reference frame [16]:

$$V_{sd} = R_s I_{sd} + \frac{d\psi_{sd}}{dt} - \omega_e \psi_{sq}$$
 (22)

$$V_{sq} = R_s I_{sq} + \frac{d\psi_{sq}}{dt} + \omega_e \psi_{sd}$$
 (23)

$$V_{rd} = R_r I_{rd} + \frac{d\psi_{rd}}{dt} - (\omega_e - \omega_r)\psi_{sq}$$
 (24)

Energies **2025**, 18, 2521 11 of 25

$$V_{rq} = R_r I_{rq} + \frac{d\psi_{rq}}{dt} + (\omega_e - \omega_r)\psi_{sd}$$
 (25)

$$\psi_{sd} = L_s I_{sd} + L_m I_{rd} \tag{26}$$

$$\psi_{sq} = L_s I_{sq} + L_m I_{rq} \tag{27}$$

$$\psi_{rd} = L_r I_{rd} + L_m I_{sd} \tag{28}$$

$$\psi_{rq} = L_r I_{rq} + L_m I_{sq} \tag{29}$$

By rearranging the previous equations with the flux linkages taken into consideration as state variables, it is simple to obtain state space representation of the d-q expression as Equation (30).

$$\frac{d}{dt} \begin{bmatrix} \psi_{ds} \\ \psi_{qs} \\ \psi_{dr} \\ \psi_{qr} \end{bmatrix} = \begin{bmatrix} \frac{-R_s}{\sigma L_s} & \omega_e & \frac{R_s L_m}{\sigma L_s L_r} & 0 \\ -\omega_e & \frac{-R_s}{\sigma L_s} & 0 & \frac{R_s L_m}{\sigma L_s L_r} \\ \frac{R_s L_m}{\sigma L_s L_r} & 0 & \frac{-R_r}{\sigma L_r} & \omega_r \\ 0 & \frac{R_s L_m}{\sigma L_s L_r} & -\omega_r & \frac{-R_r}{\sigma L_r} \end{bmatrix} \begin{bmatrix} \psi_{ds} \\ \psi_{qs} \\ \psi_{dr} \\ \psi_{qr} \end{bmatrix} + \begin{bmatrix} v_{ds} \\ v_{qs} \\ v_{dr} \\ v_{qr} \end{bmatrix}$$
(30)

If currents are utilized as state–space variables rather than fluxes, the DFIM's state-space model in the synchronous reference frame will be as Equation (31).

$$\frac{d}{dt}\begin{bmatrix} i_{ds} \\ i_{qs} \\ i_{dr} \\ i_{qr} \end{bmatrix} = \left(\frac{1}{\sigma L_s L_r}\right) \begin{bmatrix} -R_s L_r & \omega_r L_m^2 + \omega_e \sigma L_s L_r & R_r L_m & \omega_r L_m L_r \\ -\omega_r L_m^2 - \omega_e \sigma L_s L_r & -R_s L_r & -\omega_r L_m L_r & R_r L_m \\ R_s L_m & -\omega_r L_m L_r & -R_r L_s & -\omega_r L_m^2 + \omega_e \sigma L_s L_r \\ \omega_r L_m L_r & R_s L_m & \omega_r L_m^2 - \omega_e \sigma L_s L_r & -R_r L_s \end{bmatrix}$$

$$\begin{bmatrix} i_{ds} \\ i_{qs} \\ i_{dr} \\ i_{qr} \end{bmatrix} + \left(\frac{1}{\sigma L_s L_r} \right) \begin{bmatrix} L_r & 0 & -L_m & 0 \\ 0 & L_r & 0 & -L_m \\ -L_m & 0 & L_s & 0 \\ 0 & -L_m & 0 & L_s \end{bmatrix} \begin{bmatrix} v_{ds} \\ v_{qs} \\ v_{dr} \\ v_{qr} \end{bmatrix}$$
(31)

The previous arrangement is used to represent the DFIG in d-q frame since it is helpful to obtain steady state for given stator and rotor input voltages.

The electrical torque and mechanical dynamics of the system are being represented using Equations (32) and (33), respectively.

$$T_e = 3\frac{P}{2}L_m (I_{sq}I_{rd} - I_{sd}I_{rq})$$
 (32)

$$J\frac{d\omega_m}{dt} = T_e + T_{Load} - B\omega_m \tag{33}$$

where s and r represent stator and rotor quantities, respectively. L_m , L_s , and L_r are magnetizing inductance, stator, and rotor self-inductances, respectively. T_e and T_{Load} denote the electrical and load torques. B is the friction coefficient, and P indicates the pole number. ω_m denotes the mechanical speed in $\frac{rad}{s}$, and J stands for moment of inertia. Figure 9 illustrates the Simulink model of the DFIG in d-q frame.

By utilizing the quadrature component of the rotor current, the DFIG dynamic model permits control of the electromagnetic torque (I_{rq}) . This control mechanism enables the system to follow the reference speed generated by the MPPT algorithm while keeping active and reactive power under stator-flux FOC decoupled.

Energies **2025**, 18, 2521 12 of 25

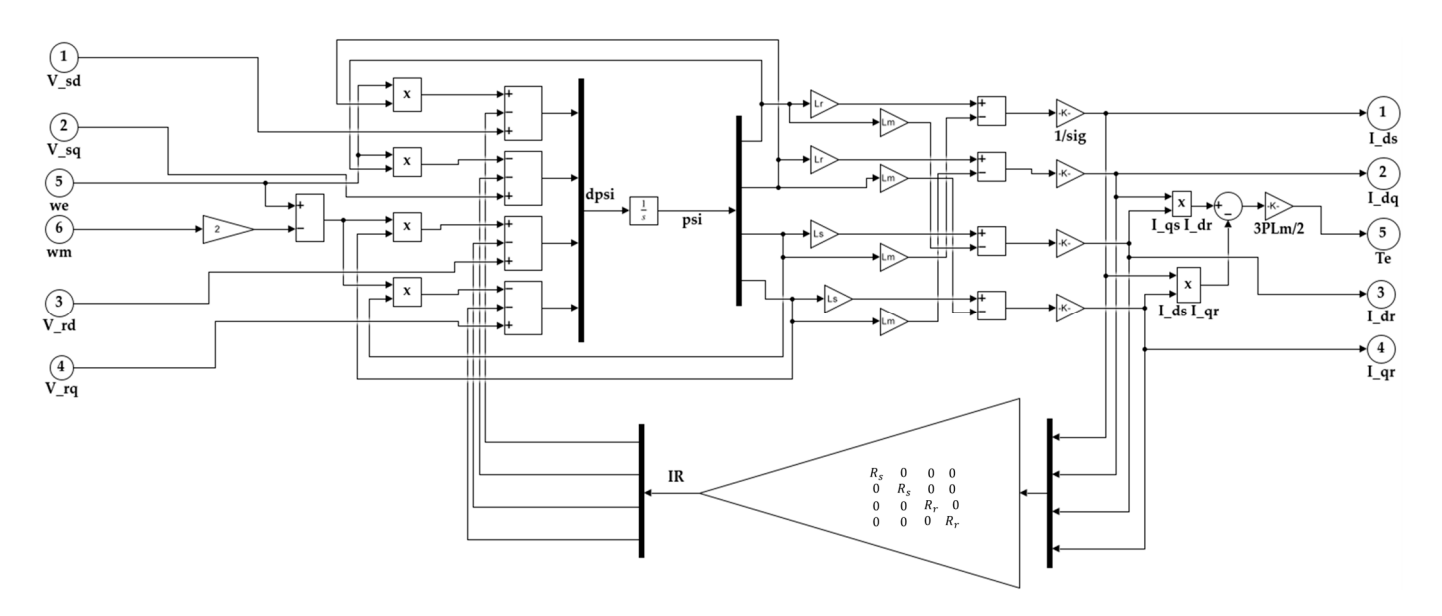


Figure 9. DFIG's Simulink model.

5. Prediction of the Shaft Speed

For the estimation of the non-linear mapping between the independent variables, which are the speed of the wind speed (V_w), the blade pitch angle (θ), and the dependent variable, which is chosen to be the turbine's shaft speed (ω_m), is the parameter whose power is to be maximized, an ANN is utilized. In neural networks, the training set for this non-linear estimation or prediction implicates the states V_w and θ as inputs and ω_m as an output. A three-layer ANN is an efficacious technique for nonlinear function prediction. Figure 10 displays this study procedure's schematic diagram.

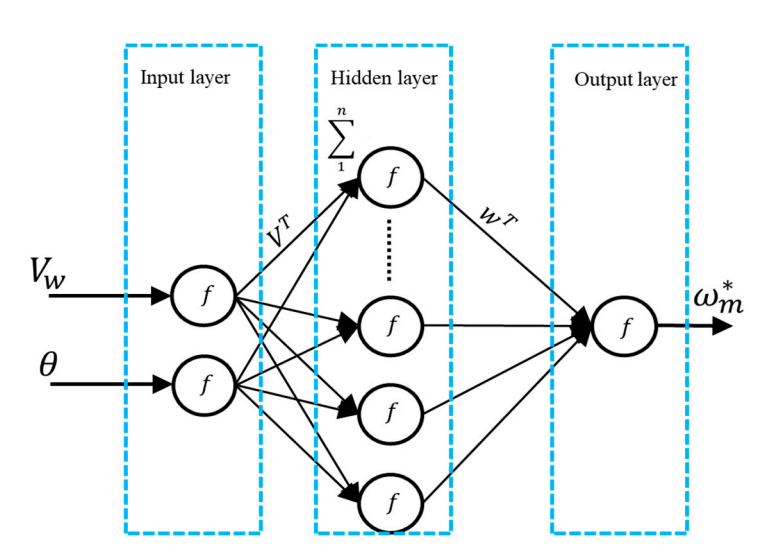


Figure 10. Neural network for predicting shaft speed.

It is essential to note that the pitch angle in this system functions not only as an aerodynamic control variable but also as a power-limiting mechanism. During the high wind, when the generator power exceeds the rated power, the pitch angle is regulated to limit the turbine's input power and indirectly reduce rotor speed. Therefore, the ANN training dataset inherently captures both normal operation and power-limited scenarios through variations in θ . By including this interaction in the training data, the ANN can accurately predict the optimal rotor speed under both unconstrained and power-limited conditions, which accordingly eliminates the need for a separate speed limiter

Energies **2025**, 18, 2521 13 of 25

To calculate the net activation a_j in a neural network, data are received by the input layer, multiplied by the relevant weights V_{ji} , and then added to a bias term b_{jo} . Equation (34) expresses the calculation of the net activation of the input layer:

$$a_j = \sum_{i=1}^{l_o} V_{ji} p_i + b_{jo} \tag{34}$$

where p_i is the input to the i^{th} node; b_{jo} is the associated bias term; and $j = 1, 2, 3 \dots lo$ denotes the hidden layer's number of neurons. An activation function f applied to the net activation value yields the hidden layer's output, which is determined by the following:

$$y_{i} = f(a_{j}) = f\left(\sum_{i=1}^{l_{o}} V_{ji} p_{i} + b_{jo}\right)$$
(35)

where f represents the activation function, selected to be hyperbolic tangent (tanh).

Then, the net activation of the output layer is calculated as Equation (36):

$$a_k = \sum_{j=1}^{l_o} W_{kj} y_i + b_{ko} (36)$$

where k represents the neuron number of the output layer, and W_{kj} represents the weight, which has a scalar value, between the j^{th} node in the hidden layer and the k^{th} node at the output layer. Based on its net activation, the output layer generates the desired shaft speed, ω_m^* as output:

$$\omega_m^* = f_1(a_k) \tag{37}$$

As expressed in Equation (38), the weights relating to the input and hidden layers V_{ji} , and the weights relating to the hidden and output layers W_{kj} , can all be used to indicate the output of the model.

$$\omega_m^* = f_1 \left(\sum_{j=1}^{l_o} W_{kj} f\left(\sum_{i=1}^n V_{ji} p_i + b_{jo} \right) + b_{ko} \right)$$
 (38)

This expression can be expressed in vector form as Equation (39):

$$\omega_m^* = \overline{f} \Big(\overline{W}^T \overline{f} \Big(\overline{V}^T \overline{p} + b_v \Big) + b_w \Big)$$
 (39)

This equation can be stated more specifically as Equation (40):

$$\omega_m^* = (W tanh(V\overline{p} + b_v) + b_w) \tag{40}$$

Once the network structure has been chosen, the mean squared error (MSE), commonly referred to as the cost function, is typically defined as Equation (41):

$$J(V_{ji}, w_{kj}) = \frac{1}{2} \sum_{i=1}^{i_o} (\omega_m - \omega_m^*)^2$$
 (41)

where ω_m the actual optimal shaft speed and ω_m^* is the ANN-predicted shaft speed.

Results from ANN Simulation

The weights of the ANN model have been modified using the Levenberg–Marquardt training procedure. Either the maximum permitted number of iterations or the MSE standard determines when the iterative process ends. To estimate an accurate shaft speed based on the training data, a range of network parameter values, such as the number

Energies **2025**, 18, 2521 14 of 25

of neurons distributed across the hidden layers, have been methodically changed. The flowchart of ANN model is given in Figure 11.

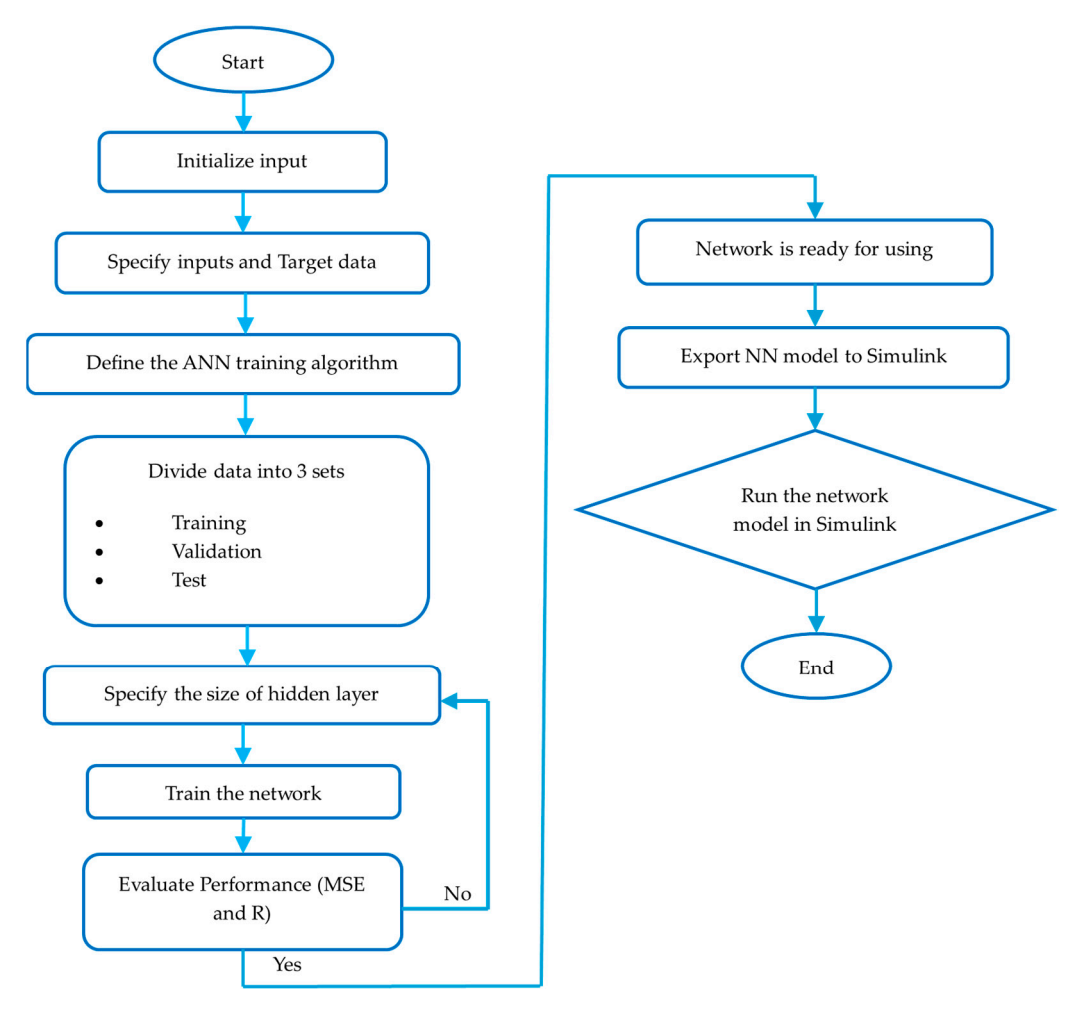


Figure 11. Flow chart of ANN.

The training data were generated by simulating a wind turbine model designed to match the 1 kW DFIG. A total of 6001 samples were generated by varying wind speed from 3 m/s to 15 m/s and pitch angle from 0° to 12° . For each combination, the optimal rotor speed was calculated by maximizing the power coefficient Cp. The dataset was randomly divided into 70% training, 15% validation, and 15% testing. ANN parameters are listed in Table 1.

Three layers make up the final ANN structure for ω_m prediction. The input variables are found in the first layer, also referred to as the input layer, contains the input variables V_w and θ . The second layer, refers to the hidden layer, contains 15 neurons. The third layer, known as the output layer, predicts the shaft speed ω_m^* that maximizes the generated power. With this selection of network parameters, the predicted and actual values match excellently.

There is a massive error at the beginning of the prediction; however, as demonstrated in Figure 12, the error decreases as the number of epochs increases. The regression plot of the ANN model has been illustrated in Figure 13. The regression value R determines if the prediction is successfully performed or needs to be trained again. It is obviously seen that R = 1, which is the optimal value of the prediction process.

Energies **2025**, 18, 2521 15 of 25

Table 1. ANN parameters.

Neuron Network Architecture	Multi-Layer Perceptron Feedforward	
Inputs	Pitch angle and wind speed	
output	Turbine Shaft speed	
Number of neurons at each layer input	2	
Hidden	15	
Output	1	
Training function (Algorithm)	(Levenberg–Marquardt algorithm)	

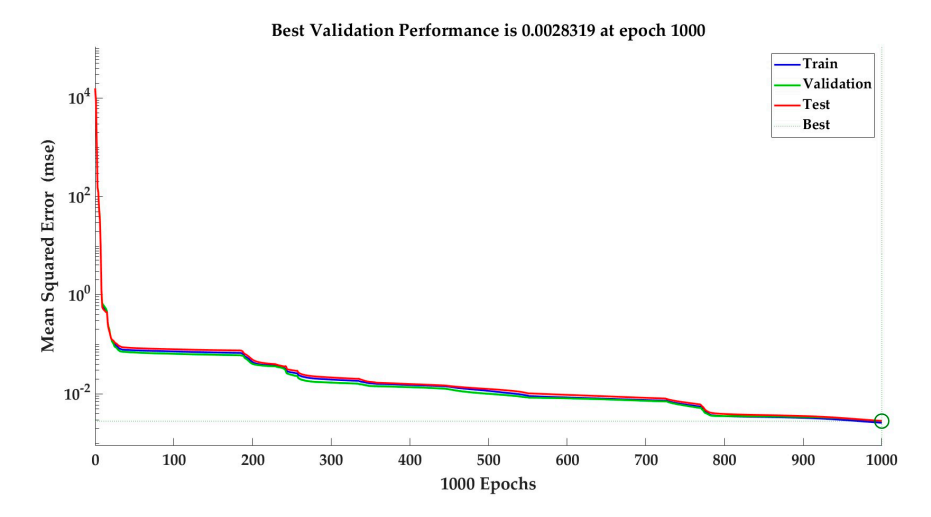


Figure 12. Performance of the ANN.

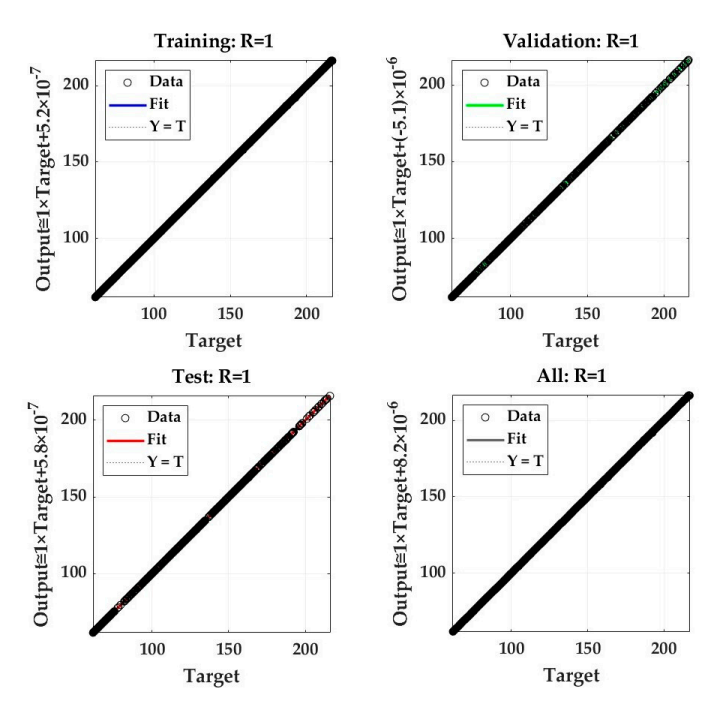


Figure 13. The regression plot of ANN.

Figure 14 displays the error histogram related to the shaft speed prediction. It displays very little inaccuracy with almost zero average value. The predicted shaft speed, which has been obtained so far, will be used as the speed reference for controlling the DFIG.

Energies **2025**, 18, 2521 16 of 25

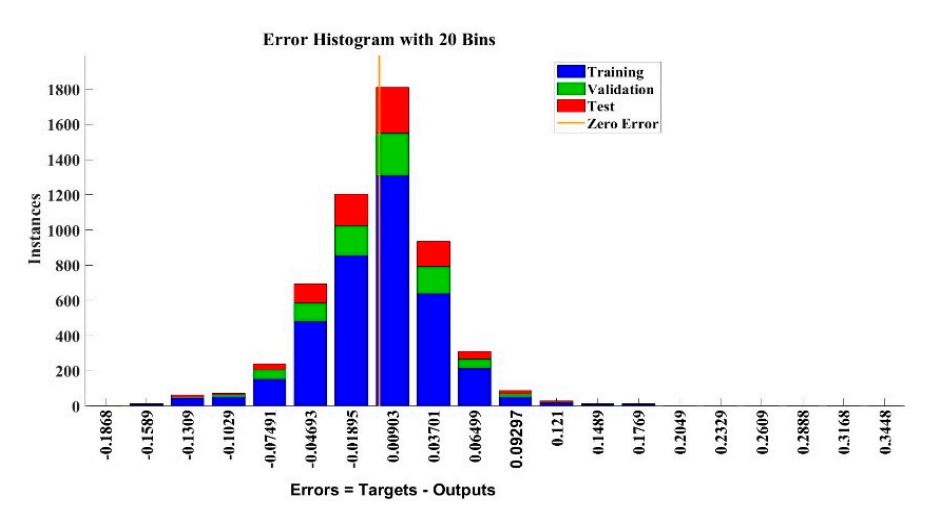


Figure 14. The errors in the histogram plot of ANN.

6. Field-Oriented Controller

The FOC method has been implemented together with the MC modulation technique for controlling the DFIG. The control has been executed in a synchronously rotating reference frame, where the flux through the windings of the stator has been aligned with the d-axis.

$$\psi_{sq} = 0$$
 and $\frac{d\psi_{rq}}{dt} = 0, \psi_{sd} = L_m I_{ms}$ and $\frac{d\psi_{rq}}{dt} = 0$

where I_{ms} is DFIG's stator magnetizing current.

By assuming the q – axis component of the stator flux to be zero, the flux is directed entirely along the d-axis. In this configuration, the rotor current's q component controls active power control, while its d component manages reactive power control. This approach will enhance the system's dynamic performance and efficiency [10].

The substantiality of the proposed control approach can be acquired by measuring the stator voltage, rotor current, and rotor mechanical speed. Then, the stator magnetizing current can be estimated as Equation (42):

$$\frac{\tau_{ms}}{I_{sm}}V_{sd} + I_{rd} = I_{ms} + \tau_{ms}\frac{dI_{ms}}{dt}$$

$$\tag{42}$$

The stator's time constant, τ_{ms} is given by $\frac{L_s}{R_s}$. The electrical angular velocity can be estimated by Equation (43):

$$\omega_e = \frac{\frac{T_{ms}}{L_m} V_{sq} + I_{rq}}{T_{ms} I_{ms}} \tag{43}$$

$$V_{rd} = R_r I_{rd} + \sigma L_r \frac{dI_{rd}}{dt} + V_{rdc} \tag{44}$$

$$V_{rq} = R_r I_{rq} + \sigma L_r \frac{dI_{rq}}{dt} + V_{rqc} \tag{45}$$

$$T_e = -3\frac{P}{2}\frac{L_m^2}{L_s}I_{ms}I_{rq} {46}$$

$$P_s = -3\omega_e \frac{L_m^2}{L_s} I_{ms} I_{rq} \tag{47}$$

$$Q_{s} = 3\omega_{e} \frac{L_{m}^{2}}{L_{s}} I_{ms} (I_{ms} - I_{rd})$$
(48)

Energies **2025**, 18, 2521 17 of 25

where σ is the leakage coefficient; P_s is the real power of the stator; and Q_s is the reactive power of the stator. Then, compensation terms, V_{rdc} and V_{rqc} , are expressed as Equations (49) and (50):

$$V_{rdc} = (1 - \sigma)L_r \frac{dI_{ms}}{dt} - (\omega_e - \omega_r)\sigma L_r I_{rq}$$
(49)

$$V_{rqc} = (\omega_e - \omega_r) \sigma L_r I_{rd} + (\omega_e - \omega_r) (1 - \sigma) L_r I_{ms}$$
(50)

The leakage coefficient is expressed by Equation (51).

$$\sigma = \frac{L_s L_r - L_m^2}{L_s L_r} \tag{51}$$

These are the equations used in the control system. Block diagram representation of the wind turbine-driven DFIG employing FOC with an ANN-based MPPT algorithm are shown in Figure 15.

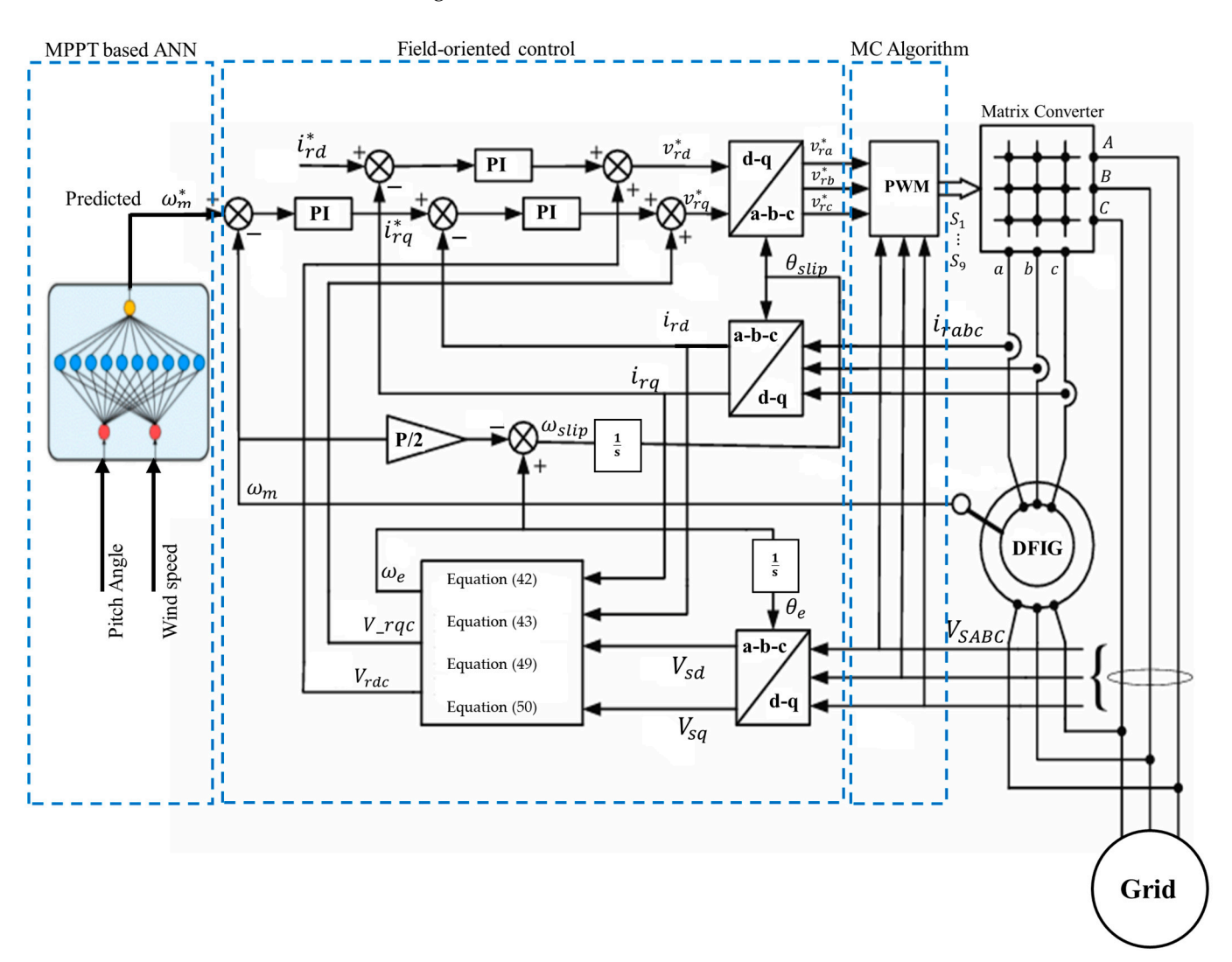


Figure 15. The diagram of the FOC.

By synthesizing the regulated rotor voltage and frequency directed by FOC method, the MC acts as the rotor-side converter, achieving decoupled active and reactive power control in the DFIG, as seen in Figure 15.

Energies **2025**, 18, 2521 18 of 25

7. Simulation Results

Simulations based on the MATLAB/Simulink environment have been carried out to assess the effectiveness and performance of the suggested control system for overall system, and the entire system model in Simulink blocks is displayed in Figure 16. The objective is to validate the impact of the ANN-based MPPT and the FOC scheme in maximizing power extraction and ensuring stable operation under variable wind conditions. The parameters of the DFIG were taken from an actual machine used in the laboratory. In order to ensure the compatibility and realistic simulation performance, the wind turbine parameters were determined to match the operational characteristics of the DFIG. Turbine and DFIG parameters are displayed in Table 2.

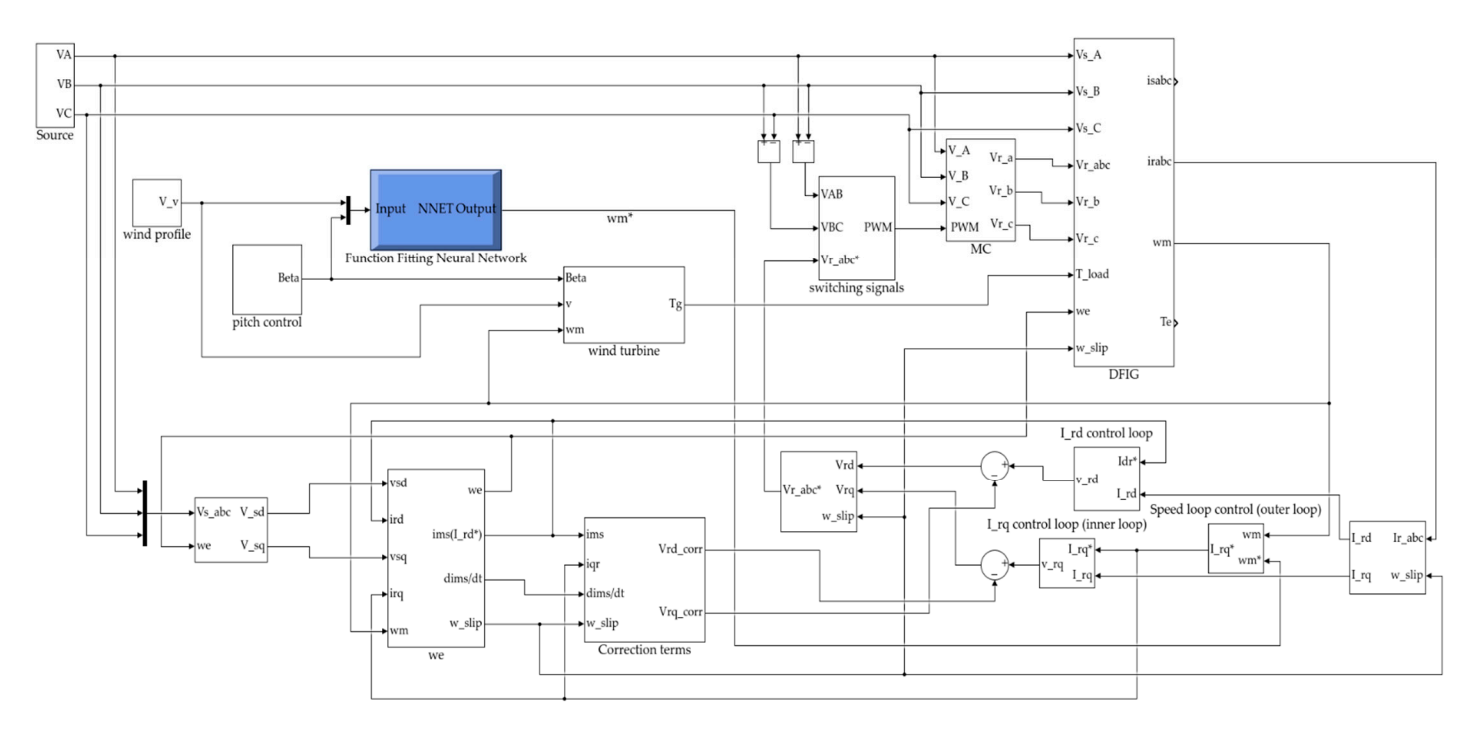


Figure 16. MATLAB/Simulink model of the entire system.

The main objective of the simulation was to assess the ANN-based MPPT performance under various wind speed situations during regular grid operation without replicating grid failures or transient disruptions.

The WECS model-based DFIG with MC has been operated at wind speeds that fluctuate over time using a pitch-angle control mechanism. Unless the power produced by the wind exceeds the generator's rated power, the value of the pitch-angle value continues to be zero. Otherwise, it would be regulated. Through the adopted control strategy, the turbine was able to achieve its optimal power by tracking the maximum value of C_p when the pitch angle is zero degrees as demonstrated in Figure 17. However, at the intervals between 22.4 and 37 s, the pitch angle was regulated due to the excess wind power generated by the turbine. This pitch angle regulation protects the turbine from severe wind powers by adjusting the C_p value.

The ANN model, which predicts or forecasts the ideal shaft speed that optimizes the power, gives the possible wind speeds and pitch angle values based on the curves of the power and speed of the wind turbine. Wind turbine shaft speed is transmitted to the generator side through the gearbox ratio. The predicted speed, which guarantees ideal tracking and MPE, is utilized as the reference speed for the DFIG's rotor. Figure 18 shows how the DFIG functions at sub-synchronous and super-synchronous speeds. The stator windings of the four-pole DFIG are connected to a 50 Hz constant voltage source. The

Energies 2025, 18, 2521 19 of 25

generator operates at super-synchronous region when the rotor speed exceeds 1500 rpm. Otherwise, it operates at sub-synchronous region.

Table 2.	The wind	turbine and	DFIG	parameters.
----------	----------	-------------	------	-------------

Turbine Parameters				
Parameters	Symbol	Value	Unit	
Length of the blade	R	0.7	m	
Air density	ρ	1.25	k_g/m^3	
Gearbox ratio	G	1.4	-	
	DFIG Pa	rameters		
The nominal power	Р	1000	W	
The number of pole pairs	p	2	-	
The stator resistance	\dot{R}_s	9.83	Ω	
The stator inductance	L_s	0.0292	Н	
The rotor resistance	R_r	8.14	Ω	
The rotor inductance	L_r	0.0292	Н	
The mutual inductance	L_m	0.4294	Н	
Inertia	j	0.01	$k_g m^2$	
Viscous friction coefficient	В	0.005	$N\overset{\circ}{\cdot}m\cdot s$	

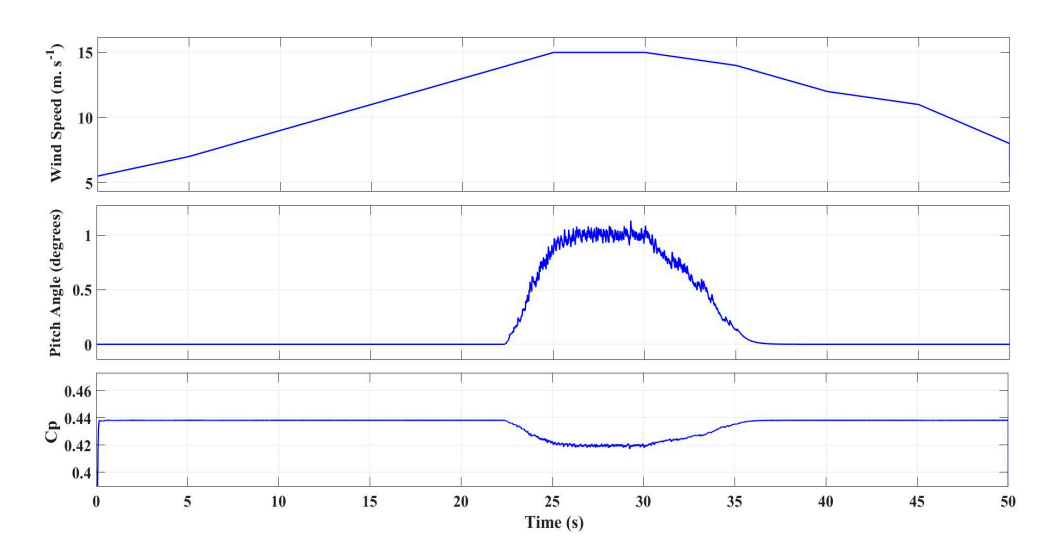


Figure 17. The power coefficient C_p , pitch angle, and wind speed profile.

DFIG power is divided into stator and rotor components. While the stator's real power P_s is always negative, indicating that it is being supplied to the main grid, the rotor's real power P_r , which depends on the rotor speed, can be either supplied to or drawn from the main grid. In Figure 19, it is seen that under sub-synchronous conditions, the power of the rotor has a positive sign, indicating that the power is being absorbed by the rotor, whereas at the super-synchronous condition, the power has a negative value, indicating the power is being delivered to the main grid. The algebraic sum of both powers will give the net power generated by the machine $P_{net} = P_s \pm P_r$, which is presented in Figure 19.

The stator's reactive power curve is illustrated in Figure 20. It has been controlled to remain zero due to the assumption that the power factor should be unity; this can be achieved according to Equation (48) by setting the reference of the current I_{rd} to be equal to the magnetizing stator current I_{ms} . However, in cases where reactive power is needed to be delivered to the main grid, the current I_{rd} will be increased to be more than the magnetizing current; this is performed by multiplying the reference current by a factor that makes it

Energies **2025**, 18, 2521 20 of 25

above the magnetizing current I_{ms} . The reference value of q component of rotor current I_{rq} is obtained from the output of speed controller loop.

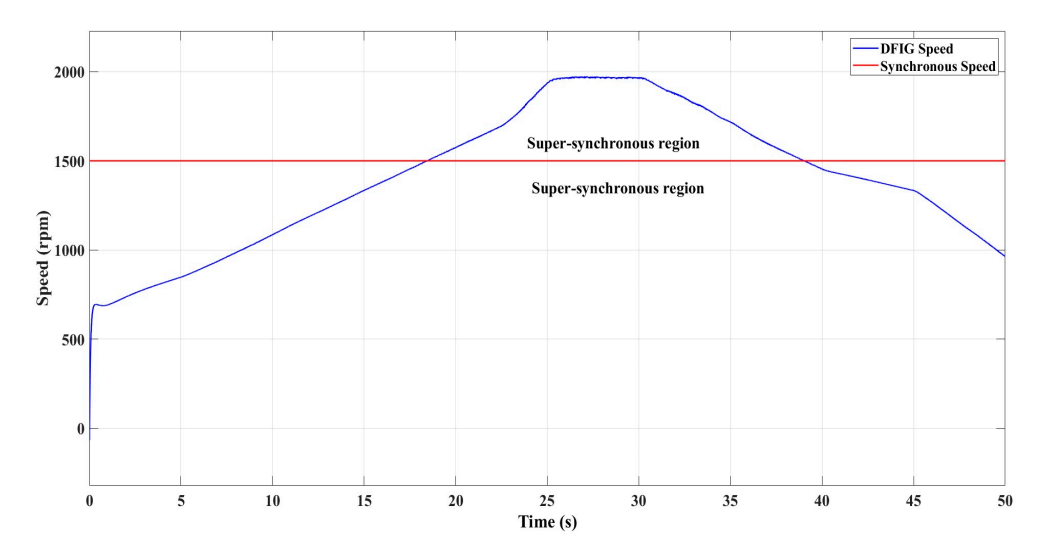


Figure 18. The speed of DFIG.

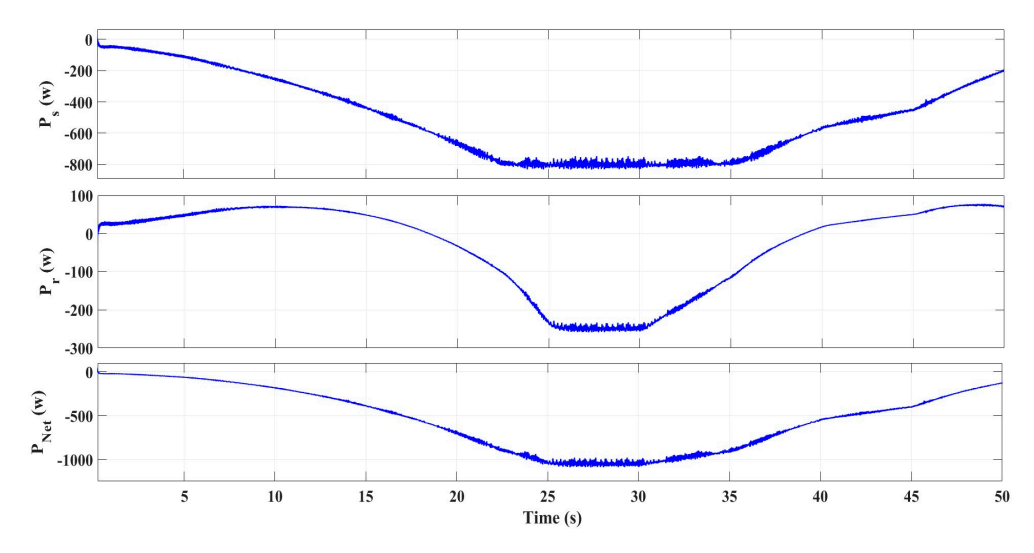


Figure 19. The DFIG stator power P_s , rotor power P_r , and net power P_{net} .

In Figure 21, as long as the stator's reactive power is kept at zero, there will be a phase angle of 180° between the voltage of the main grid and DFIG's stator current, indicating the pure real power exchange by the stator side, ensuring that it is operating with power factor of unity. Additionally, despite the variation in the rotor speed, the stator current frequency stays fixed at 50 Hz because it is connected to the main grid directly.

Figure 22 demonstrates the waveforms of the MC input current and the grid phase voltage during sub-synchronous operation region of the DFIG. During this region, the waveforms will be in phase, which indicates that the rotor of the machine is absorbing power from the main grid. However, in Figure 23, it has been illustrated that while the DFIG operates in the super-synchronous region, there will be a phase shift of 180° between the voltage and current, indicating the power is being transmitted from the rotor to the grid over MC.

Energies **2025**, 18, 2521 21 of 25

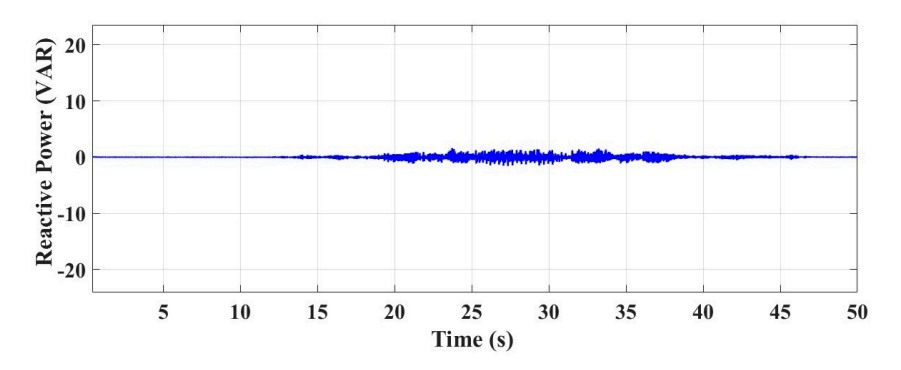


Figure 20. The stator reactive power.

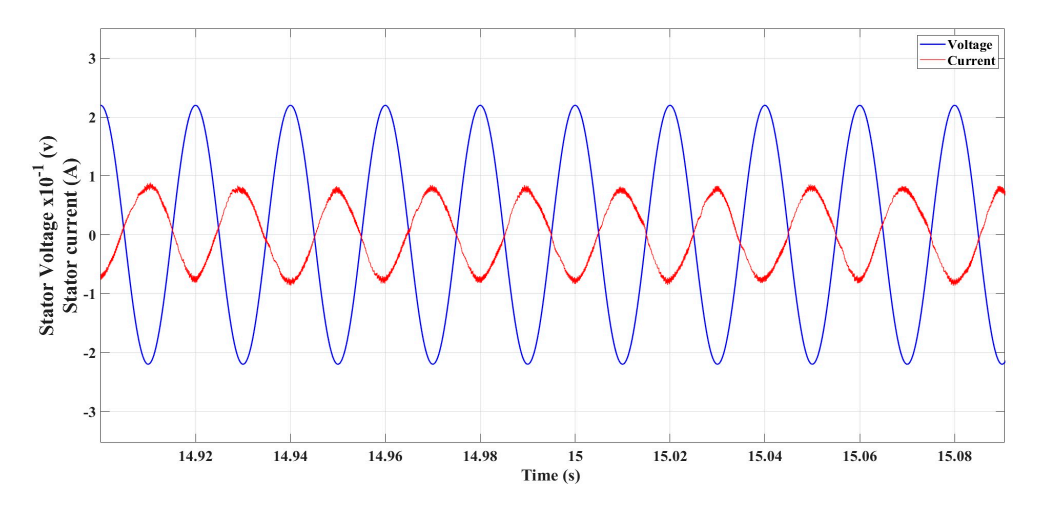


Figure 21. The grid phase voltage and its corresponding phase current waveforms.

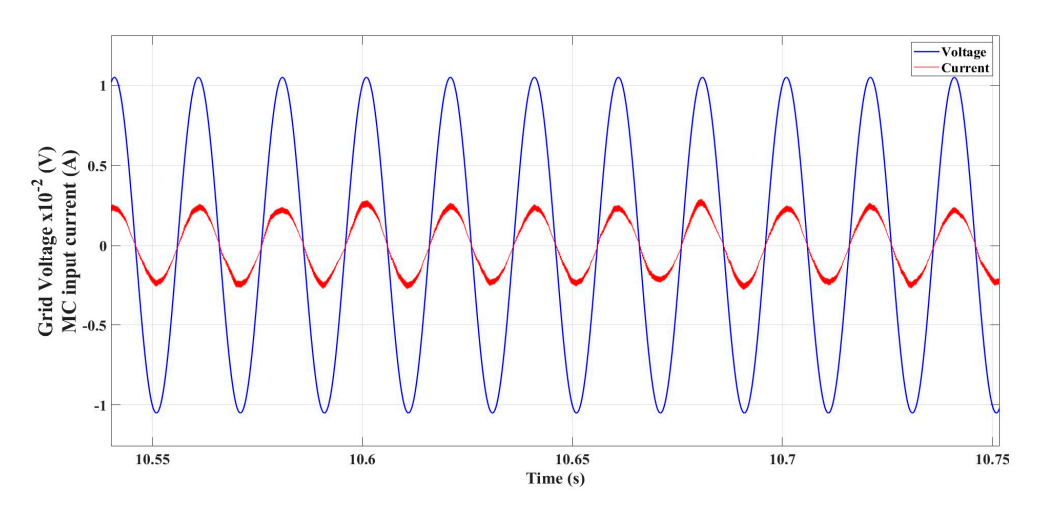


Figure 22. Waveforms of grid phase voltage and MC input current in a sub-synchronous region.

The simulation results confirm that the MC successfully maintained the decoupled active and reactive power control by effectively supplying the necessary rotor-side voltage and frequency, allowing for bidirectional power flow in a range of wind conditions.

Furthermore, a comparison between the suggested ANN-based MPPT and a traditional 2D lookup table-based MPPT, which was developed in [10], was conducted. The tracking performance of the power coefficient (Cp) for both approaches at different wind speeds is shown in Figure 24.

Energies **2025**, 18, 2521 22 of 25

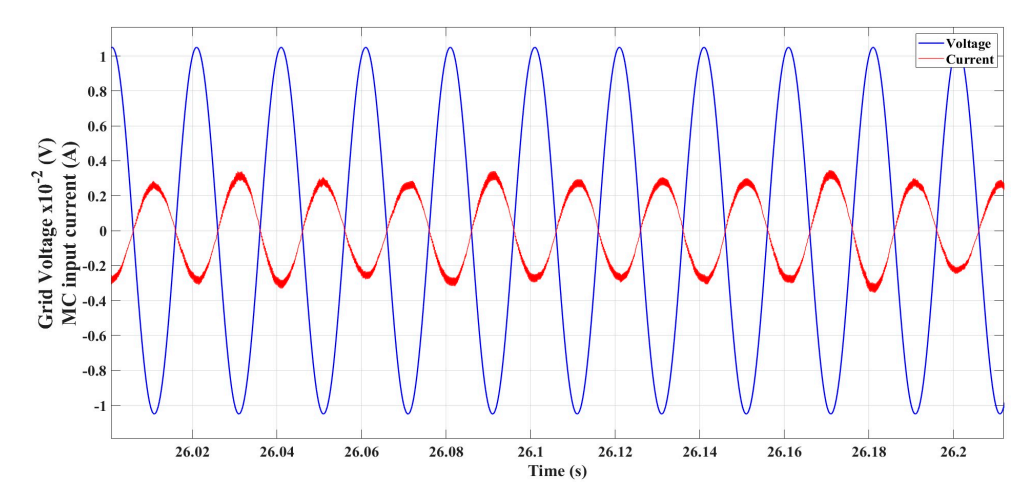


Figure 23. Waveforms of grid phase voltage and MC input current in super-synchronous region.

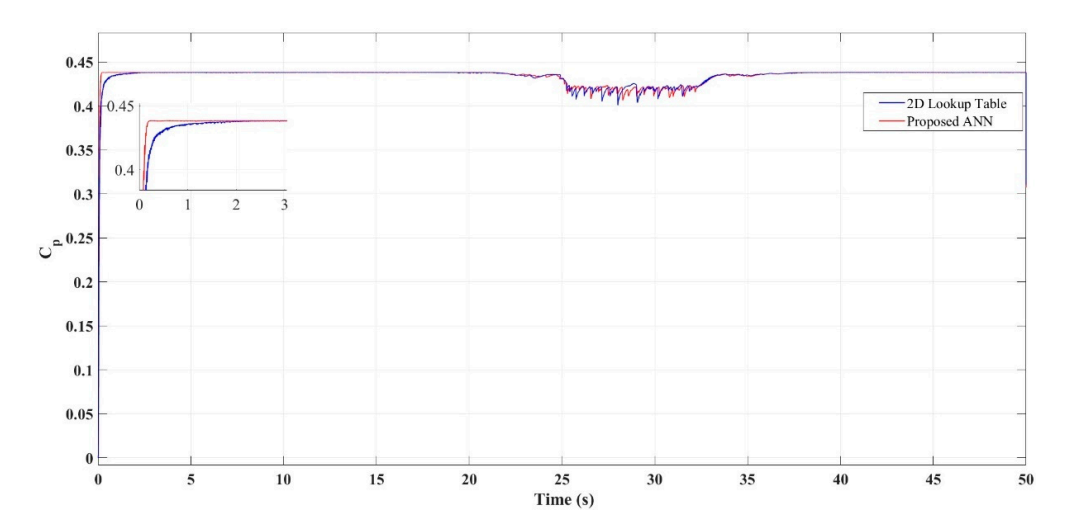


Figure 24. Comparison of power coefficient (Cp) tracking using the proposed ANN-based MPPT and the conventional 2D lookup table method under varying wind speeds.

In comparison to the 2D lookup table technique, the findings show that the ANN-based MPPT achieves faster convergence to the optimal Cp and maintains superior tracking accuracy especially in transient regions. Table 3 provides a summary of a comparison study to further illustrate the benefits of the suggested ANN-based MPPT over the traditional 2D lookup table-based MPPT developed in [10]. This table outlines key differences in adaptability, performance, and implementation aspects between the two approaches, demonstrating the improvements achieved by the proposed method.

Energies **2025**, 18, 2521 23 of 25

MPPT Method	2D Lookup Table [10]	ANN
Data Requirement	Requires offline-generated lookup table	Trained once; no real-time lookup needed
Adaptability to parameter changes	Limited (static table)	High (ANN can generalize to unseen data)
Convergence speed to C _p max	Slower	Faster
Control Complexity	Moderate	Slightly higher (due to ANN)
Need for updating data	Requires manual update if parameters change	Self-adaptive after retraining
Memory requirements	Higher (due to table storage)	Lower
Simulation Tool	MATLAB/Simulink	MATLAB/Simulink

Table 3. Comparison between ANN-based and lookup table-based MPPT approaches.

8. Conclusions

The design, control, and simulation of the grid-connected WECS are presented in this article. The ANN technique has been used to predict the shaft speed that extracts the maximum possible power from the wind. By utilizing an ANN model, the system dynamically predicts the shaft speed based on the speed of the wind and pitch angle to ensure the extraction of maximum power. The simulation results have illustrated that the usage of the ANN improves adaptability; moreover, it obtains accurate and efficient power tracking under variable wind conditions. Furthermore, it offered faster convergence to the optimal power coefficient and a smoother dynamic response compared to the conventional 2D lookup table method.

There are several benefits using the MC in the rotor side of DFIG as compared to conventional back-to-back converters. Whereby, the need for DC-link capacitors has been removed with the MC, increasing system reliability by lowering the number of elements. It also enables bidirectional power flow, which allows the dynamic transfer of energy between the main grid and rotor of the DFIG in both sub-synchronous and super-synchronous regions. Furthermore, the MC ensures sinusoidal input and output waveforms at both sides, which minimizes harmonic distortion and improves power quality. The simulation results highlight that the combination of ANN-based MPPT together with MC offers a compact, effective, and high-performance solution for DFIG-based WECSs.

Future works might concentrate on putting the proposed control system into real-time hardware. Further investigation will focus on the ANN-based MPPT's scalability for utility-scale turbines, the integration of advanced machine learning models to increase adaptability under rapidly changing situations, and the incorporation of fault detection and diagnostic capabilities to improve system resilience and reliability.

Author Contributions: Conceptualization, M.A.A. and S.S.; formal analysis, S.S.; investigation, M.A.A. and S.S.; methodology, M.A.A.; project administration, S.S.; resources, S.S.; software, M.A.A. and S.S.; supervision, S.S.; validation, M.A.A. and S.S.; writing—original draft, M.A.A.; writing—review and editing, S.S. All authors have read and agreed to the published version of the manuscript.

Funding: This research received no external funding.

Data Availability Statement: The original contributions presented in this study are included in the article. Further inquiries can be directed to the corresponding author.

Conflicts of Interest: The authors declare no conflicts of interest.

Energies **2025**, 18, 2521 24 of 25

References

1. Olabi, A.G.; Obaideen, K.; Abdelkareem, M.A.; AlMallahi, M.N.; Shehata, N.; Alami, A.H.; Mdallal, A.; Hassan, A.A.M.; Sayed, E.T. Wind Energy Contribution to the Sustainable Development Goals: Case Study on London Array. *Sustainability* **2023**, *15*, 4641. [CrossRef]

- Haq, I.U.; Khan, Q.; Khan, I.; Akmeliawati, R.; Nisar, K.S.; Khan, I. Maximum Power Extraction Strategy for Variable Speed Wind Turbine System via Neuro-Adaptive Generalized Global Sliding Mode Controller. IEEE Access 2020, 8, 128536–128547. [CrossRef]
- 3. Bekiroglu, E.; Yazar, M.D. MPPT Control of Grid Connected DFIG at Variable Wind Speed. Energies 2022, 15, 3146. [CrossRef]
- 4. Patel, R.; Hafiz, F.; Swain, A.; Ukil, A. Nonlinear Rotor Side Converter Control of DFIG Based Wind Energy System. *Electr. Power Syst. Res.* **2021**, *198*, 107358. [CrossRef]
- 5. Aljafari, B.; Pamela Stephenraj, J.; Vairavasundaram, I.; Singh Rassiah, R. Steady State Modeling and Performance Analysis of a Wind Turbine-Based Doubly Fed Induction Generator System with Rotor Control. *Energies* **2022**, *15*, 3327. [CrossRef]
- 6. Boukhezzar, B.; Siguerdidjane, H. Comparison between Linear and Nonlinear Control Strategies for Variable Speed Wind Turbines. *Control Eng. Pract.* **2010**, *18*, 1357–1368. [CrossRef]
- 7. Barzegar-Kalashani, M.; Seyedmahmoudian, M.; Mekhilef, S.; Stojcevski, A.; Horan, B. Small-Scale Wind Turbine Control in High-Speed Wind Conditions: A Review. *Sustain. Energy Technol. Assess.* **2023**, *60*, 103577. [CrossRef]
- 8. Le, X.C.; Duong, M.Q.; Le, K.H. Review of the Modern Maximum Power Tracking Algorithms for Permanent Magnet Synchronous Generator of Wind Power Conversion Systems. *Energies* **2022**, *16*, 402. [CrossRef]
- 9. Pande, J.; Nasikkar, P.; Kotecha, K.; Varadarajan, V. A Review of Maximum Power Point Tracking Algorithms for Wind Energy Conversion Systems. *J. Mar. Sci. Eng.* **2021**, *9*, 1187. [CrossRef]
- Altun, H.; Sünter, S. Modeling, Simulation and Control of Wind Turbine Driven Doubly-Fed Induction Generator with Matrix Converter on the Rotor Side. *Electr. Eng.* 2013, 95, 157–170. [CrossRef]
- 11. Elumalai, R. Maximum power quality tracking of artificial neural network controller-based double fed induction generator for wind energy conversion system. *Rev. Roum. Sci. Tech.*—Ser. Électrotechnique Énergetique **2024**, 69, 189–194. [CrossRef]
- 12. Arnaltes, S.; Rodriguez-Amenedo, J.; Montilla-DJesus, M. Control of Variable Speed Wind Turbines with Doubly Fed Asynchronous Generators for Stand-Alone Applications. *Energies* **2017**, *11*, 26. [CrossRef]
- 13. Yousefzadeh, M.; Ahmadi Kamarposhti, M. Wind Energy Conversion Systems: A Review on Aerodynamic, Electrical and Control Aspects, Recent Trends, Comparisons and Insights. In *Energy and Environmental Aspects of Emerging Technologies for Smart Grid*; Springer: Cham, Switzerland, 2024; pp. 25–60.
- 14. Camblong, H.; de Alegria, I.M.; Rodriguez, M.; Abad, G. Experimental Evaluation of Wind Turbines Maximum Power Point Tracking Controllers. *Energy Convers. Manag.* **2006**, 47, 2846–2858. [CrossRef]
- 15. Lalouni, S.; Rekioua, D.; Idjdarene, K.; Tounzi, A. Maximum Power Point Tracking Based Hybrid Hill-Climb Search Method Applied to Wind Energy Conversion System. *Electr. Power Compon. Syst.* **2015**, *43*, 1028–1038. [CrossRef]
- Kumar, S.S.; Jayanthi, K.; Kumar, N.S. Maximum Power Point Tracking for a PMSG Based Variable Speed Wind Energy Conversion System Using Optimal Torque Control. In Proceedings of the 2016 International Conference on Advanced Communication Control and Computing Technologies (ICACCCT), Ramanathapuram, India, 25–27 May 2016; pp. 347–352.
- 17. Mahfoud, S.; Derouich, A.; Iqbal, A.; El Ouanjli, N. ANT-Colony Optimization-Direct Torque Control for a Doubly Fed Induction Motor: An Experimental Validation. *Energy Rep.* **2022**, *8*, 81–98. [CrossRef]
- 18. Chetouani, E.; Errami, Y.; Obbadi, A.; Sahnoun, S.; Chojaa, H. Optimization Power Control for Rotor Side Converter of a DFIG Using PSO Evolutionary Algorithm. In *Digital Technologies and Applications, Proceedings of the ICDTA*'22, Fez, Morocco, 28–29 *January* 2022; Springer: Cham, Switzerland, 2022; pp. 541–551.
- 19. Guediri, A.; Hettiri, M.; Guediri, A. Modeling of a Wind Power System Using the Genetic Algorithm Based on a Doubly Fed Induction Generator for the Supply of Power to the Electrical Grid. *Processes* **2023**, *11*, 952. [CrossRef]
- Ali, A.; Irshad, K.; Khan, M.F.; Hossain, M.M.; Al-Duais, I.N.A.; Malik, M.Z. Artificial Intelligence and Bio-Inspired Soft Computing-Based Maximum Power Plant Tracking for a Solar Photovoltaic System under Non-Uniform Solar Irradiance Shading Conditions—A Review. Sustainability 2021, 13, 10575. [CrossRef]
- 21. Mohamed, A.Z.; Eskander, M.N.; Ghali, F.A. Fuzzy Logic Control Based Maximum Power Tracking of a Wind Energy System. *Renew. Energy* **2001**, *23*, 235–245. [CrossRef]
- 22. Sathish Babu, P.; Sundarabalan, C.K.; Balasundar, C.; Santhana Krishnan, T. Fuzzy Logic Based Optimal Tip Speed Ratio MPPT Controller for Grid Connected WECS. *Mater. Today Proc.* **2021**, *45*, 2544–2550. [CrossRef]
- 23. Ro, K.; Choi, H. Application of Neural Network Controller for Maximum Power Extraction of a Grid-Connected Wind Turbine System. *Electr. Eng.* **2005**, *88*, 45–53. [CrossRef]
- 24. Tabrizi, Y.H.; Uddin, M.N. Multi-Agent Reinforcement Learning-Based Maximum Power Point Tracking Approach to Fortify PMSG-Based WECSs. *IEEE Trans. Ind. Appl.* **2024**, *60*, 8077–8087. [CrossRef]

Energies **2025**, 18, 2521 25 of 25

25. Chhipa, A.A.; Kumar, V.; Joshi, R.R.; Chakrabarti, P.; Jasinski, M.; Burgio, A.; Leonowicz, Z.; Jasinska, E.; Soni, R.; Chakrabarti, T. Adaptive Neuro-Fuzzy Inference System-Based Maximum Power Tracking Controller for Variable Speed WECS. *Energies* 2021, 14, 6275. [CrossRef]

- 26. Zribi, M.; Alrifai, M.; Rayan, M. Sliding Mode Control of a Variable-Speed Wind Energy Conversion System Using a Squirrel Cage Induction Generator. *Energies* **2017**, *10*, 604. [CrossRef]
- 27. Mahvash, H.; Taher, S.A.; Rahimi, M.; Shahidehpour, M. Enhancement of DFIG Performance at High Wind Speed Using Fractional Order PI Controller in Pitch Compensation Loop. *Int. J. Electr. Power Energy Syst.* **2019**, *104*, 259–268. [CrossRef]
- 28. Bossanyi, E.A. The Design of Closed Loop Controllers for Wind Turbines. Wind Energy 2000, 3, 149-163. [CrossRef]
- 29. Kalbat, A. Linear Quadratic Gaussian (LQG) Control of Wind Turbines. In Proceedings of the 2013 3rd International Conference on Electric Power and Energy Conversion Systems, Istanbul, Turkey, 2–4 October 2013; pp. 1–5.
- 30. Daili, Y.; Gaubert, J.-P.; Rahmani, L.; Harrag, A. Quantitative Feedback Theory Design of Robust MPPT Controller for Small Wind Energy Conversion Systems: Design, Analysis and Experimental Study. *Sustain. Energy Technol. Assess.* **2019**, *35*, 308–320. [CrossRef]
- 31. Rezaei, V. Advanced Control of Wind Turbines: Brief Survey, Categorization, and Challenges. In Proceedings of the 2015 American Control Conference (ACC), Chicago, IL, USA, 1–3 July 2015; pp. 3044–3051.
- 32. Farrar, N.; Ali, M.H. Cyber-Resilient Converter Control System for Doubly Fed Induction Generator-Based Wind Turbine Generators. *Electronics* **2024**, *13*, 492. [CrossRef]
- 33. Mahmud, T.; Gao, H. A Comprehensive Review on Matrix-Integrated Single-Stage Isolated MF/HF Converters. *Electronics* **2024**, 13, 237. [CrossRef]
- 34. Shapoval, I.; Clare, J.; Chekhet, E. Experimental Study of a Matrix Converter Excited Doubly-Fed Induction Machine in Generation and Motoring. In Proceedings of the 2008 13th International Power Electronics and Motion Control Conference, Poznan, Poland, 1–3 September 2008; pp. 307–312.
- 35. Cardenas, R.; Pena, R.; Tobar, G.; Clare, J.; Wheeler, P.; Asher, G. Stability Analysis of a Wind Energy Conversion System Based on a Doubly Fed Induction Generator Fed by a Matrix Converter. *IEEE Trans. Ind. Electron.* **2009**, *56*, 4194–4206. [CrossRef]
- 36. Benbouhenni, H.; Bizon, N. Advanced Direct Vector Control Method for Optimizing the Operation of a Double-Powered Induction Generator-Based Dual-Rotor Wind Turbine System. *Mathematics* **2021**, *9*, 2403. [CrossRef]
- 37. Abad, G.; López, J.; Rodríguez, M.A.; Marroyo, L.; Iwanski, G. *Doubly Fed Induction Machine*; Wiley: Hoboken, NJ, USA, 2011; ISBN 9780470768655.
- 38. Sierra-Garcia, J.E.; Santos, M.; Pandit, R. Wind Turbine Pitch Reinforcement Learning Control Improved by PID Regulator and Learning Observer. *Eng. Appl. Artif. Intell.* **2022**, 111, 104769. [CrossRef]
- 39. Reyes, V.; Rodriguez, J.J.; Carranza, O.; Ortega, R. Review of Mathematical Models of Both the Power Coefficient and the Torque Coefficient in Wind Turbines. In Proceedings of the 2015 IEEE 24th International Symposium on Industrial Electronics (ISIE), Buzios, Brazil, 3–5 June 2015; pp. 1458–1463.
- 40. Venturini, M. New Sine Wave in, Sine Wave out Conversion Technique Eliminates Reactive Elements. In Proceedings of the Powercon 7, San Diego, CA, USA, 24–27 March 1980; pp. E3.1–E3.15.
- 41. Alesina, A.; Venturini, M. Solid-State Power Conversion: A Fourier Analysis Approach to Generalized Transformer Synthesis. *IEEE Trans. Circuits Syst.* **1981**, *28*, 319–330. [CrossRef]
- 42. Sünter, S. Slip Energy Recovery of a Rotor-Side Field Oriented Controlled Wound Rotor Induction Motor Fed by Matrix Converter. *J. Frankl. Inst.* **2008**, 345, 419–435. [CrossRef]
- 43. Narayanaswamy, P.R. Iyer Modelling, Simulation and Real-Time Implementation of a Three-Phase AC to AC Matrix Converter. Ph.D. Thesis, Curtin University, Perth, Australia, 2012.
- 44. Altun, H.; Sunter, S. Matrix Converter Induction Motor Drive: Modeling, Simulation and Control. *Electr. Eng. (Arch. Elektrotechnik)* **2003**, *86*, 25–33. [CrossRef]

Disclaimer/Publisher's Note: The statements, opinions and data contained in all publications are solely those of the individual author(s) and contributor(s) and not of MDPI and/or the editor(s). MDPI and/or the editor(s) disclaim responsibility for any injury to people or property resulting from any ideas, methods, instructions or products referred to in the content.